International Journal of Mechanical Sciences 314 (2026) 111343

Contents lists available at ScienceDirect

International Journal of Mechanical Sciences

journal homepage: www.elsevier.com/locate/ijmecsci

Stabilized HEPM for large-deformation hydro-mechanics in saturated porous media

Yuanyi Qiu, Zhen-Yu Yin *, Huangcheng Fang

Department of Civil and Environmental Engineering, The Hong Kong Polytechnic University, Hung Hom, Kowloon, Hong Kong, China
State Key Laboratory of Climate Resilience for Coastal Cities, The Hong Kong Polytechnic University, Hong Kong, China

ARTICLE INFO

Keywords:
Hybrid Element Particle Method
Porous media
Large deformation
Nonlinear consolidation
Pressure stabilization

ABSTRACT

The accurate prediction of hydro-mechanical interactions in saturated soils is essential for assessing the stability of critical geotechnical infrastructure. However, modeling the coupled hydro-mechanical response of saturated soils involving large deformations presents a significant computational challenge, primarily due to the limitations of traditional grid-based methods in handling severe mesh distortion. The core of the proposed HEPM lies in its dual spatial discretization, which decouples the material motion from the numerical mesh. The physical continuum is discretized by a collection of particles that store all state variables, along with an auxiliary mesh used to construct the particle interpolation. Formulated within an Updated Lagrangian (UL) framework based on Biot's theory, the method incorporates a particle-based Finite Increment Calculus (FIC) stabilization technique. This ensures the suppression of spurious pressure oscillations, thereby enabling the use of efficient equal-order interpolations for both solid displacement and pore pressure. The accuracy and robustness of the proposed method are validated through a series of benchmark tests, showing excellent agreement with analytical solutions for consolidation problems and highlighting its versatility in handling complex material nonlinearities, including nonlinear hydraulic behaviors. Ultimately, the results demonstrate the capability of the proposed framework to reliably solve complex failure problems in computational geomechanics, offering a robust numerical strategy that effectively overcomes mesh distortion and numerical instability in large-deformation hydro-mechanical analysis.

1. Introduction

The numerical analysis of coupled hydro-mechanical large deformations in saturated porous media is essential for modern geotechnical engineering, enabling the prediction of critical phenomena such as landslides [1,2], foundation settlement [3–5], and complex soil–structure interactions [6,7]. However, modeling these problems presents a significant challenge. This difficulty arises from the inherent nonlinear coupling between the solid skeleton deformation and the pore fluid flow, a complexity that is further amplified by geometric nonlinearities [8,9], especially for soft foundations. Thereby, a robust numerical framework capable of handling these combined physical complexities is essential for reliable analysis.

Among the various numerical techniques for these problems, the Finite Element Method (FEM) is the prevailing standard in computational solid mechanics [10,11] and, more specifically, in geotechnical engineering [12–14]. The widespread application of FEM is due to its robust framework, which is well-suited to the complexities of geomaterials, including the analysis of hydro-mechanical coupling [15–18] and the enforcement of complex boundary conditions [19–21]. However, the standard Lagrangian approach faces a central weakness in problems involving large deformation. Severe mesh distortion, degrades accuracy, leads to ill-conditioned system matrices, and ultimately causes computation failure [22]. To address this limitation, several alternative approaches have been proposed. One widely used method is the Arbitrary Lagrangian–Eulerian (ALE) method, which mitigates mesh distortion by decoupling mesh motion from material movement [23–25]. However, the ALE method has notable disadvantages. Specifically, both the mesh and the material require independent sets of degrees of freedom, which introduces additional variables that must be tracked and solved during the simulation [26]. This increase in degrees of freedom leads to higher computational costs and greater complexity in numerical implementation. Another powerful approach for large-deformation geomechanics is the Stabilized Node-based Smoothed Particle Finite Element Method (SNS-PFEM) [27,28]. This method integrates a dynamic remeshing

* Corresponding author at: Department of Civil and Environmental Engineering, The Hong Kong Polytechnic University, Hung Hom, Kowloon, Hong Kong, China.
E-mail address: zhenyu.yin@polyu.edu.hk (Z.-Y. Yin).

https://doi.org/10.1016/j.ijmecsci.2026.111343
Received 29 September 2025; Received in revised form 29 January 2026; Accepted 31 January 2026
Available online 3 February 2026
0020-7403/© 2026 The Authors. Published by Elsevier Ltd. This is an open access article under the CC BY license (http://creativecommons.org/licenses/by/4.0/).

scheme with node-based strain smoothing, which effectively resolves mesh distortion issues while enhancing strain field accuracy. However, despite these advantages, the reliance on a complete remeshing at each step introduces significant practical and algorithmic challenges. The process of nodal re-connectivity for mesh generation is highly complex and particularly in three-dimensional analyses, the regenerated tetrahedral elements may contain slivers, which can compromise numerical accuracy and stability. Moreover, the reliance on an external alpha-shape algorithm for boundary identification is both computationally intensive and complex to implement [29,30].

An alternative strategy is to abandon the mesh structure entirely. In particle-based methods, the problem domain is represented as a collection of interacting particles. A prominent example is Smoothed Particle Hydrodynamics (SPH). As a fully Lagrangian method, SPH is powerfully adapted for porous media problems by using separate sets of interacting particles to represent the solid skeleton and the pore water [31–35]. Its primary advantage is the inherent ability to handle extreme deformations and coupled water flow without any possibility of mesh distortion. However, for complex geotechnical boundary value problems, SPH faces challenges in accurately imposing boundary conditions [36], suffers from potential tensile instability [37–39], limiting its application. Moreover, the Element-Free Galerkin (EFG) method, a meshless approach using moving least-squares approximations, is particularly adept at simulating large deformations due to its independence from a fixed mesh [40,41]. However, this advantage is offset by significant computational demands. The method requires computationally intensive procedures, such as neighborhood searches and the assembly of shape functions, which increase both implementation complexity and overall computational cost.

Seeking to combine the accuracy and boundary condition handling of mesh-based methods with the robustness of particle methods for large deformations, hybrid formulations have gained attention. A leading example is the Material Point Method (MPM), an advanced hybrid technique particularly well-suited for geotechnical porous media problems [42–45]. MPM utilizes a collection of material points to represent the soil skeleton and pore fluid. Simultaneously, the governing equations of motion and fluid flow are solved on a stationary background grid. This dual framework elegantly avoids mesh distortion, making it increasingly popular for large-deformation geotechnical analysis, including consolidation [46,47]. However, MPM faces inherent challenges, notably the quadrature errors arising from degraded particle distributions and the cell-crossing noise triggered by discontinuous shape function gradients as particles traverse element boundaries [48–50]. As a robust alternative for large-deformation analysis, the Hybrid Element Particle Method (HEPM) [51,52] fundamentally overcomes these limitations. Distinguished from traditional hybrid methods by its dual discretization and dynamic remeshing strategy, HEPM reconstructs interpolation functions based on the current particle position. This approach ensures the continuity of field gradients, thereby intrinsically overcoming the cell-crossing noise and quadrature errors in MPM. Furthermore, unlike the SNS-PFEM, where mesh generation is constrained by the connectivity of moving nodes, often leading to poor element quality [53], HEPM reconstructs the background mesh arbitrarily based on the current domain configuration. This flexibility ensures consistently high-quality elements throughout the simulation.

In numerical simulations of hydro-mechanical problems, ensuring a stable pore pressure field is a significant challenge, particularly when approaching the undrained incompressible limit—conditions characterized by low permeability and rapid loading. Stability is governed by the discrete inf–sup (or LBB) condition, which must be satisfied by the interpolation functions chosen for solid displacement (u) and pore pressure (p) [54]. Using an unstable interpolation pair, such as equal-order elements, violates this condition and leads to non-physical, spurious oscillations in the pressure field, rendering the numerical solution inaccurate [55]. This challenge motivates the development of dedicated stabilization techniques that permit the use of simple and computationally efficient equal-order elements for both displacement and pressure. Various strategies exist, including polynomial pressure projection method in SNS-PFEM [56,57], nodal averaging schemes in MPM [58,59]. Moreover, the Finite Increment Calculus (FIC) framework offers an effective approach to ensure numerical stability in FEM [60–62], introducing stabilization terms derived directly from the balance equations that inherently stabilize the pressure field for equal-order linear elements. It can ensure numerical stability in the incompressible limit while preserving the algorithmic simplicity and computational efficiency of linear background elements. Since the proposed HEPM is based on a dual discretization of background mesh and particles, the FIC stabilization strategies can theoretically and naturally be adapted to the current framework.

Building upon the kinematic framework of HEPM recently developed for large-deformation solid mechanics [51], this study extends the method to a fully coupled hydro-mechanical formulation for saturated porous media. The primary objective is to establish a stabilized coupling framework capable of rigorously analyzing large-deformation hydro-mechanical problems involving elasto-plasticity. A linearization of the coupled governing equations is derived, which fully accounts for both geometric and material nonlinearities. Furthermore, a particle-based FIC stabilization technique is implemented to enable the use of computationally efficient equal-order interpolation, while a finite strain constitutive model and a nonlinear permeability law are incorporated to capture the complex consolidation behavior of soft soils. The performance of the proposed method is rigorously validated against several analytical solutions and demanding numerical examples, demonstrating its robustness and accuracy in predicting both settlement and pore pressure dissipation.

The remainder of this paper is structured as follows. Section 2 details the theoretical foundation, covering the governing equations for porous media, the consistent linearization for large deformation, the core theory of HEPM, the evolution of hydraulic properties, and the remeshing strategy. Section 3 then briefly introduces the implementation of this particle-based FIC-stabilized method within the HEPM framework. Subsequently, Section 4 is dedicated to verification and validation. This section first assesses the performance in terms of pore pressure evolution and spatial convergence against analytical solutions for consolidation problems. In addition, the robustness of the HEPM is evaluated through challenging large-strain elasto-plastic simulations, including strip footing and vertical cutting of soil block. Finally, Section 5 summarizes and concludes the paper.

2. Methodology and formulation

This section presents the equations of the hydro-mechanical coupling algorithm based on the Hybrid Element Particle Method (HEPM), specifically formulated to overcome mesh distortion in quasi-static, large-deformation nonlinear consolidation. These equations are developed within an updated Lagrangian framework to accurately capture geometric nonlinearities, building upon the foundational principles of Biot's theory of poroelasticity [63]. Moreover, the particle-based interpolation and gradient reconstruction strategy of the proposed HEPM is also introduced, which allows field variable derivatives to be computed robustly at the particle level.

2.1. Governing equations in porous media

The behavior of saturated porous media is governed by the coupling between the solid skeleton deformation and the pore fluid flow. Adopting a quasi-static formulation where inertial terms are neglected [16], the linear momentum balance for the mixture is expressed alongside the effective stress principle as:

$$\nabla \cdot \boldsymbol{\sigma} + \rho \mathbf{b} = \mathbf{0}, \quad \text{with} \quad \boldsymbol{\sigma} = \boldsymbol{\sigma}' - \alpha p \mathbf{I}, \tag{1}$$

where $\boldsymbol{\sigma}$ and $\boldsymbol{\sigma}'$ are the total and effective stress tensors, respectively, $\mathbf{b}$ is the body force vector, ρ is the density of the mixture, p is the pore water pressure, α is the Biot coefficient, and $\mathbf{I}$ is the identity matrix. The conservation of fluid mass involves the fluid density ρ_w, porosity n, and Darcy velocity $\mathbf{v}$. Assuming the fluid flow follows Darcy's law $\mathbf{v} = -(\mathbf{k}/\mu_w)(\nabla p - \rho_w \mathbf{g})$ and the fluid is weakly compressible defined by the bulk modulus K_w, the governing equation for fluid flow in saturated porous media is derived as:

$$\left(\frac{\alpha - n}{K_s} + \frac{n}{K_w}\right)\frac{\partial p}{\partial t} + \alpha \nabla \cdot \dot{\mathbf{u}} + \nabla \cdot \left[\frac{\mathbf{k}}{\mu_w}\left(-\nabla p + \rho_w \mathbf{g}\right)\right] = Q, \tag{2}$$

where K_s is the bulk modulus of the solid grains, $\mathbf{k}$ is the intrinsic permeability tensor, and Q represents the fluid source. To account for large-deformation behavior, the volumetric strain rate $\nabla \cdot \dot{\mathbf{u}}$ is equivalent to $\dot{J}/J$, where $\dot{J}$ represents the rate of volume change and J denotes the Jacobian determinant defined as the ratio of the current volume to the reference volume ($V^{t+\Delta t}/V^t$). Finally, the system is closed with a prescribed flux boundary condition on Γ_w, expressed as $(\mathbf{k}/\mu_w)(-\nabla p + \rho_w \mathbf{g}) \cdot \mathbf{n} = q_w$, where $\mathbf{n}$ is the unit normal vector and q_w is the prescribed volumetric flux per unit area.

2.2. HEPM discretization

Building upon the large-deformation variational formulation detailed in Appendix A, the core of the HEPM framework involves reconstructing element interpolation to enable particle-based approximation [51]. The fundamental principle relies on a dual discretization of the domain into an auxiliary finite element mesh and a set of Lagrangian particles, allowing the coupled governing equations to be transformed into a particle-based system.

2.2.1. Spatial discretization of particle

The key feature of the HEPM is the spatial discretization of the problem domain using a set of Lagrangian particles, with their field variables interpolated from an auxiliary mesh. The flowchart of this coupling method is illustrated in Fig. 1. The particle interpolation scheme establishes a robust connection between the mesh-based field (represented by Gaussian points) and the particle field. The properties of a particle are calculated by integrating information from a collection of neighboring Gaussian points, which collectively form the support domain of that particle. This domain consists of a discrete set of surrounding Gaussian points at which the kernel function has non-zero values. To define this relationship, each Gaussian point is assigned a spherical influence domain to identify the particles it affects. Since the radius of the influence domain can vary for each Gaussian point, the resulting support domain for a particle is typically irregular in shape rather than being a fixed sphere. To manage the neighbor search process efficiently, a spatial partitioning algorithm like the KD-Tree method is employed, which organizes particles into a hierarchical tree structure based on a space division diagram. Ultimately, all physical quantities for a particle, such as its lumped volume, strain, and pressure, are computed via a weighted average of the corresponding values from the Gaussian points within its support domain. In the first step, the volume V_k for each Gaussian point on an auxiliary mesh is computed using its weight w_k:

$$V_k = w_k \det(\mathbf{Jac}_k) \quad \text{with} \quad \mathbf{Jac}_k = \frac{\partial \mathbf{N}^e}{\partial \boldsymbol{\xi}} \mathbf{x}^e \Big| \boldsymbol{\xi} = \boldsymbol{\xi}_k, \quad k = 1, 2, \ldots, n_g, \tag{3}$$

where $\mathbf{Jac}_k$ is the Jacobian matrix at the kth Gaussian point, calculated using the nodal coordinate $\mathbf{x}^e$ of element e and the derivatives of shape function $\mathbf{N}^e$ at the local coordinate of kth Gaussian point; n_g is the number of Gaussian points within element e.

This volume is used to define an effective radius r_k for each Gaussian point, assuming it occupies a spherical influence domain $r_k = \sqrt[3]{\frac{3V_k}{4\pi}}$. The interaction between a particle p and a Gaussian point k is quantified by a dimensionless weight coefficient φ_{pk}. This coefficient is calculated in two steps. First, an interaction function ϕ_{pk} is computed using a cubic spline kernel, which is dependent on the normalized distance d_{pk} between the particle and the Gaussian point:

$$\phi_{pk} = \begin{cases} \frac{2}{3} - 4\left(d_{pk}^2 - d_{pk}^3\right), & 0 \le d_{pk} < 0.5 \\ \frac{1}{6}(2 - 2d_{pk})^3, & 0.5 \le d_{pk} < 1 \\ 0, & d_{pk} \ge 1 \end{cases} \quad \text{with} \quad d_{pk} = \frac{\| \mathbf{x}_p - \mathbf{x}_k \|}{\eta r_k}, \tag{4}$$

where η is a constant scaling factor, typically taken as 2; ϕ_{pk} is normalized across all particles interacting with Gaussian point k, yielding the final kernel coefficient φ_{pk}:

$$\varphi_{pk} = \frac{\phi_{pk}}{\sum_{j=1}^{n_k^p} \phi_{jk}}, \tag{5}$$

where n_k^p is the number of particles within the influence domain of Gaussian point k. This normalization ensures that the coefficients φ_{pk} strictly satisfy the partition of unity at each Gaussian point k, thereby allowing the lumped volume of particle p to be consistently calculated from the neighboring Gaussian volumes V_k:

$$\sum_{p=1}^{n_k^p} \varphi_{pk} = 1 \quad \text{and} \quad V_p = \sum_{k=1}^{n_p^g} \varphi_{pk} V_k, \tag{6}$$

where n_k^p denotes the number of particles influencing Gaussian point k, and n_p^g is the number of Gaussian points within the support domain of particle p.

2.2.2. Gradient reconstruction

In the finite element method, the displacement gradient at any point within an element can be determined from the nodal displacements of that element. This calculation is typically performed at Gaussian points to facilitate numerical integration for the element stiffness matrix. The displacement gradient $\nabla \mathbf{u}(\mathbf{x}_k)$ at a Gaussian point k within an element e can be calculated from nodal displacement of element, $\mathbf{u}^e$:

$$\nabla \mathbf{u}(\mathbf{x}_k) = \mathbf{L}_k \mathbf{u}^e \quad \text{with} \quad \mathbf{L}_k = \frac{\partial \mathbf{N}^e}{\partial \boldsymbol{\xi}} \frac{\partial \boldsymbol{\xi}}{\partial \mathbf{x}}\Big|_{\boldsymbol{\xi} = \boldsymbol{\xi}_k}, \quad k = 1, 2, \ldots, n_g, \tag{7}$$

where n_g is the total number of Gaussian points. For a linear tetrahedral element with a single Gaussian integration point, the nodal displacement vector $\mathbf{u}^e$ and the vectorized gradient tensor $\nabla \mathbf{u}$ are defined as:

$$\begin{aligned} \mathbf{u}^e &= [u_{1x}, u_{1y}, u_{1z}, u_{2x}, u_{2y}, u_{2z}, u_{3x}, u_{3y}, u_{3z}, u_{4x}, u_{4y}, u_{4z}]^T, \\ \nabla \mathbf{u} &= \left[\frac{\partial u_x}{\partial x}, \frac{\partial u_x}{\partial y}, \frac{\partial u_x}{\partial z}, \frac{\partial u_y}{\partial x}, \frac{\partial u_y}{\partial y}, \frac{\partial u_y}{\partial z}, \frac{\partial u_z}{\partial x}, \frac{\partial u_z}{\partial y}, \frac{\partial u_z}{\partial z}\right]^T. \end{aligned} \tag{8}$$

The matrix $\mathbf{L}_k$ is constructed as a block matrix, defined as $\mathbf{L}_k = [\mathbf{L}_k^1, \mathbf{L}_k^2, \mathbf{L}_k^3, \mathbf{L}_k^4]$, by assembling four 9×3 sub-matrices where each $\mathbf{L}_k^i$ is derived from the partial derivatives of the shape function N_i associated with the ith node:

$$\mathbf{L}_k^i = \begin{bmatrix} N_{i,x} & N_{i,y} & N_{i,z} & 0 & 0 & 0 & 0 & 0 & 0 \\ 0 & 0 & 0 & N_{i,x} & N_{i,y} & N_{i,z} & 0 & 0 & 0 \\ 0 & 0 & 0 & 0 & 0 & 0 & N_{i,x} & N_{i,y} & N_{i,z} \end{bmatrix}^T. \tag{9}$$

After computing the $\nabla \mathbf{u}(\mathbf{x}_k)$ of Gaussian point k, the smoothed gradient at particle p, $\tilde{\nabla} \mathbf{u}_p$, is obtained by the weighted average:

$$\tilde{\nabla} \mathbf{u}_p = \frac{\sum_{k=1}^{n_p^g} \varphi_{pk} V_k \nabla \mathbf{u}(\mathbf{x}_k)}{\sum_{k=1}^{n_p^g} \varphi_{pk} V_k} = \frac{1}{V_p} \sum_{k=1}^{n_p^g} \varphi_{pk} V_k \mathbf{L}_k \mathbf{u}_k^e = \tilde{\mathbf{L}}_p \mathbf{u}_p, \tag{10}$$

where $\tilde{\mathbf{L}}_p$ is the resulting particle gradient operator for particle p, which maps the nodal displacements $\mathbf{u}_k^e$ associated with Gauss point k surrounding the particle to the gradient $\tilde{\nabla} \mathbf{u}_p$:

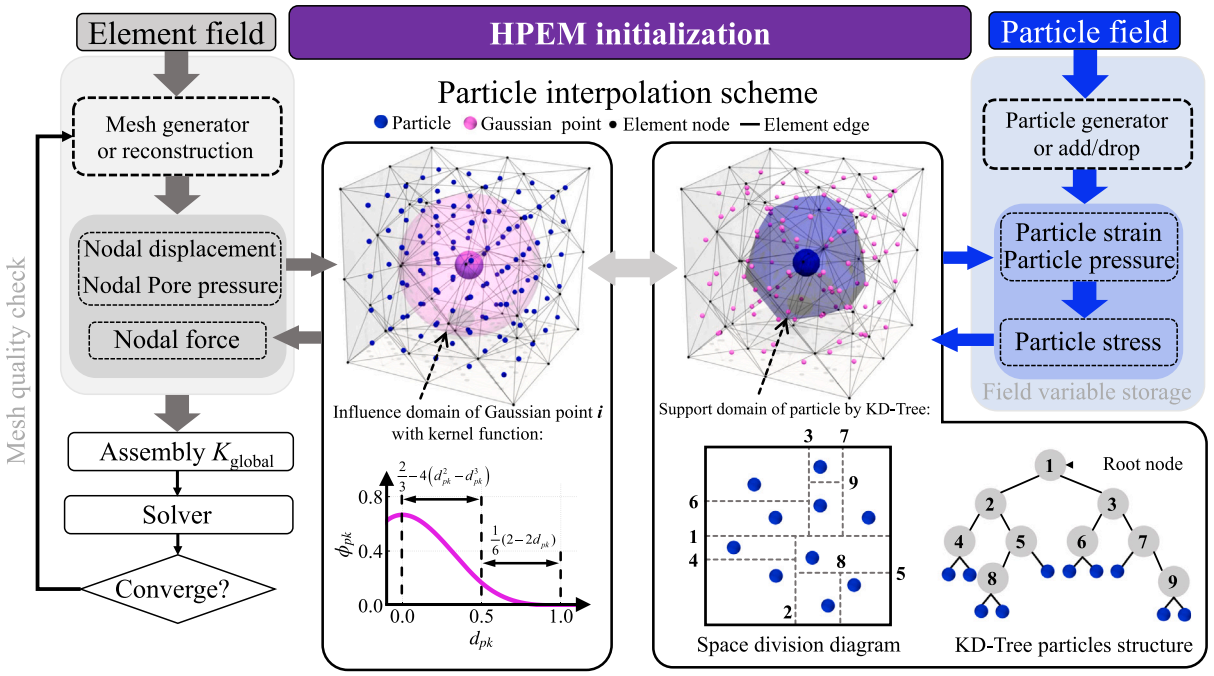

Fig. 1. Computational framework of the proposed HEPM coupling algorithm. The method utilizes a dual discretization scheme: an auxiliary finite element mesh for solving governing equations and Lagrangian particles for tracking history variables. The schematic illustrates the particle interpolation scheme, where neighboring particles for each Gauss point are identified via a KD-Tree search.

$$\tilde{\mathbf{L}}_p = \frac{1}{V_p}\left[\varphi_{p1}V_1\mathbf{L}_1 \quad \cdots \quad \varphi_{pn_p^g}V_{n_p^g}\mathbf{L}_{n_p^g}\right] \text{ and } \mathbf{u}_p = \begin{bmatrix} \mathbf{u}_1^e & \cdots & \mathbf{u}_{n_p^g}^e \end{bmatrix}. \tag{11}$$

Moreover, the particle-field divergence of the displacement, $\tilde{\nabla}\cdot\mathbf{u}_p$, can be computed by applying the same weighted averaging scheme:

$$\tilde{\nabla}\cdot\mathbf{u}_p = \frac{\sum_{k=1}^{n_p^g}\varphi_{pk}V_k\nabla\cdot\mathbf{u}(\mathbf{x}_k)}{\sum_{k=1}^{n_p^g}\varphi_{pk}V_k} = \frac{1}{V_p}\sum_{k=1}^{n_p^g}\varphi_{pk}V_k\mathbf{B}_k\mathbf{u}_k^e = \tilde{\mathbf{B}}_p\mathbf{u}_p, \tag{12}$$

with

$$\mathbf{B}_k = [(\nabla N_1)^T,(\nabla N_2)^T,(\nabla N_3)^T,(\nabla N_4)^T] \text{ and } (\nabla N_i)^T = \left[\frac{\partial N_i}{\partial x},\frac{\partial N_i}{\partial y},\frac{\partial N_i}{\partial z}\right], \tag{13}$$

where $\tilde{\mathbf{B}}_p$ is particle divergence operator, Following the structure of the particle gradient operator $\tilde{\mathbf{L}}_p$, $\tilde{\mathbf{B}}_p$ is defined as:

$$\tilde{\mathbf{B}}_p = \frac{1}{V_p}\left[\varphi_{p1}V_1\mathbf{B}_1 \quad \cdots \quad \varphi_{pn_p^g}V_{n_p^g}\mathbf{B}_{n_p^g}\right]. \tag{14}$$

Similarly, the pressure at a particle, $\tilde{p}_p$, is interpolated from the nodal pressures of the surrounding elements using nodal pressure $\mathbf{p}_k^e$:

$$\tilde{p}_p = \frac{\sum_{k=1}^{n_p^g}\varphi_{pk}V_k p(\mathbf{x}_k)}{\sum_{k=1}^{n_p^g}\varphi_{pk}V_k} = \frac{1}{V_p}\sum_{k=1}^{n_p^g}\varphi_{pk}V_k\mathbf{N}_k\mathbf{p}_k^e = \tilde{\mathbf{N}}_{pp}\mathbf{P}_p, \tag{15}$$

where $\mathbf{N}_k$ is the shape functions in pressure field, $p(\mathbf{x}_k)$ is the pore pressure at the Gaussian points, and $\tilde{\mathbf{N}}_{pp}$ is the resulting shape function matrix for particle p:

$$\tilde{\mathbf{N}}_{pp} = \frac{1}{V_p}\left[\varphi_{p1}V_1\mathbf{N}_1 \quad \cdots \quad \varphi_{pn_p^g}V_{n_p^g}\mathbf{N}_{n_p^g}\right] \text{ and } \mathbf{P}_p = \begin{bmatrix} \mathbf{p}_1^e & \cdots & \mathbf{p}_{n_p^g}^e \end{bmatrix}, \tag{16}$$

and the particle gradient of pressure, $\tilde{\nabla}p_p$, is defined as:

$$\tilde{\nabla}p_p = \tilde{\nabla}\mathbf{N}_{pp}\mathbf{P}_p \text{ with } \tilde{\nabla}\mathbf{N}_{pp} = \frac{1}{V_p}\left[\varphi_{p1}V_1\nabla\mathbf{N}_1 \quad \cdots \quad \varphi_{pn_p^g}V_{n_p^g}\nabla\mathbf{N}_{n_p^g}\right]. \tag{17}$$

2.2.3. Discretized governing equations

By applying the HEPM spatial discretization and particle-based integration, the equilibrium equations can be obtained by integrating over the collection of particles. The momentum equation Eq. (A.10) can be rewritten as:

$$\sum_{p=1}^{n}\tilde{\nabla}^{t+\Delta t}\delta\mathbf{u}_p^{[i]} : \left\{\mathbf{C}_p^{[i]} : \tilde{\nabla}^{t+\Delta t}(\Delta\mathbf{u}_p^{[i]}) - \alpha\Delta p^{[i]}\mathbf{I} + \left(\tilde{\sigma}_p^{t+\Delta t}\right)^{[i]}\left[\tilde{\nabla}^{t+\Delta t}\cdot\Delta\mathbf{u}_p^{[i]} - \left(\tilde{\nabla}^{t+\Delta t}\Delta\mathbf{u}_p^{[i]}\right)^T\right]\right\} \cdot V_p^{[i]} = (\mathbf{r}^{t+\Delta t})^{[i]}, \tag{18}$$

with

$$(\mathbf{r}^{t+\Delta t})^{[i]} = \mathbf{F}_{ext}^{[i]} - \sum_{p=1}^{n}\tilde{\nabla}^{t+\Delta t}\delta\mathbf{u}_p^{[i]} : \left(\tilde{\sigma}^{t+\Delta t}\right)^{[i]}V_p^{[i]}, \tag{19}$$

where n is the total number of particles, and the subscript p denotes a variable at the particle level. For simplicity, the subscript is omitted for the particle pore pressure, which is denoted simply as p. Given incompressible flow, the mass conservation equation Eq. (A.19) can be expressed as:

$$\begin{aligned}&\sum_{p=1}^{n}\delta p^{[i]}\alpha\tilde{\nabla}^{t+\Delta t}\cdot(\Delta\mathbf{u}_p^{[i]})V_p^{[i]} + \Delta t\sum_{p=1}^{n}(\tilde{\nabla}^{t+\Delta t}\delta p^{[i]})\cdot\frac{\mathbf{k}_p}{\mu_w}\cdot(\tilde{\nabla}^{t+\Delta t}\Delta p^{[i]})V_p^{[i]}\\ &+\Delta t\sum_{p=1}^{n}(\tilde{\nabla}^{t+\Delta t}\delta p^{[i]})\cdot\frac{\mathbf{k}_p}{\mu_w}\cdot\tilde{\nabla}^{t+\Delta t}p^{[i]}(\tilde{\nabla}^{t+\Delta t}\cdot\Delta\mathbf{u}_p)^{[i]}V_p^{[i]}\\ &-\Delta t\sum_{p=1}^{n}(\tilde{\nabla}^{t+\Delta t}\delta p^{[i]})\cdot\frac{\mathbf{k}_p}{\mu_w}\cdot\left[\tilde{\nabla}^{t+\Delta t}\Delta\mathbf{u}_p^{[i]} + (\tilde{\nabla}^{t+\Delta t}\Delta\mathbf{u}_p^{[i]})^T\right]\cdot\tilde{\nabla}^{t+\Delta t}p^{[i]}V_p^{[i]} = (\mathbf{R}_p^{t+\Delta t})^{[i]},\end{aligned} \tag{20}$$

with

$$(\mathbf{R}_p^{t+\Delta t})^{[i]} = \Delta t\mathbf{F}_p^{[i]} - \sum_{p=1}^{n}\delta p^{[i]}\alpha\left(\frac{J-1}{J}\right)^{[i]}V_p^{[i]} - \Delta t\sum_{p=1}^{n}\tilde{\nabla}^{t+\Delta t}\delta p^{[i]}\cdot\frac{\mathbf{k}_p}{\mu_w}\tilde{\nabla}^{t+\Delta t}(p^{t+\Delta t})^{[i]}V_p^{[i]}. \tag{21}$$

The external load vector $\mathbf{F}_{ext}^{[i]}$ and source term $\mathbf{F}_p^{[i]}$ are computed on the background mesh via the standard FEM. Then, substituting the particle displacement gradient Eq. (11) and pore pressure Eq. (16) into the

governing equations yields the final form of the system equations:

$$\begin{aligned}&\mathbf{K}_{C\&S}^{[i]}\Delta\mathbf{u}-\mathbf{Q}_P{}^{[i]}\Delta\mathbf{p}=\mathbf{F}_{ext}^{[i]}-\mathbf{F}_{int}^{[i]},\\&[(\mathbf{Q}_P^{[i]})^T+\Delta t\mathbf{Q}_{nl}^{[i]}]\Delta\mathbf{u}^{[i]}+\Delta t\mathbf{H}_P^{[i]}\Delta\mathbf{p}^{[i]}=\mathbf{R}_P^{[i]},\end{aligned}\tag{22}$$

where $\Delta\mathbf{u}$ and $\Delta\mathbf{p}$ are the vectors of incremental nodal displacements and pore pressures, respectively. The stiffness matrix $\mathbf{K}_{C\&S}$, the coupling matrix $\mathbf{Q}_{\mathrm{P}}$, the nonlinear coupling matrix $\mathbf{Q}_{\mathrm{nl}}$, and the permeability matrix $\mathbf{H}_{\mathrm{P}}$ are given as follows:

$$\begin{aligned}\mathbf{K}_{C\&S}^{[i]}&=\sum_{p=1}^{n}\left(\tilde{\mathbf{L}}_p^{[i]}\right)^T\left(\mathbf{C}+\mathbf{S}^{t+\Delta t}\right)^{[i]}\tilde{\mathbf{L}}_p^{[i]}V_p^{[i]},\\\mathbf{Q}_P^{[i]}&=\sum_{p=1}^{n}\left(\tilde{\mathbf{B}}_p^{[i]}\right)^T\alpha\tilde{\mathbf{N}}_{pp}^{[i]}V_p^{[i]},\\\mathbf{Q}_{nl}^{[i]}&=\sum_{p=1}^{n}\left(\tilde{\nabla}\mathbf{N}_{pp}^{[i]}\right)^T\frac{\mathbf{k}_p^{t+\Delta t}}{\mu_w}\cdot\left[\tilde{\nabla}(p^{t+\Delta t})^{[i]}\tilde{\mathbf{B}}_p^{[i]}-\boldsymbol{\Gamma}(\tilde{\nabla}(p^{t+\Delta t})^{[i]})\tilde{\mathbf{L}}_p^{[i]}\right],\\\mathbf{H}_P^{[i]}&=\sum_{p=1}^{n}\left(\tilde{\nabla}\mathbf{N}_{pp}^{[i]}\right)^T\frac{\mathbf{k}_p^{t+\Delta t}}{\mu_w}\tilde{\nabla}\mathbf{N}_{pp}^{[i]}V_p^{[i]},\\\mathbf{F}_{int}^{[i]}&=\sum_{p=1}^{n}\left(\tilde{\mathbf{L}}_p^{[i]}\right)^T\left(\tilde{\boldsymbol{\sigma}}_p^{t+\Delta t}\right)^{[i]}V_p^{[i]},\\\mathbf{R}_P^{[i]}&=\Delta t(\mathbf{F}_P^{[i]})-\mathbf{F}_Q^{[i]}-\mathbf{F}_H^{[i]},\\\mathbf{F}_Q^{[i]}&=\sum_{p=1}^{n}\left(\tilde{\mathbf{N}}_{pp}^{[i]}\right)^T\alpha(V_p^{t+\Delta t}-V_p^t)^{[i]},\\\mathbf{F}_H^{[i]}&=\Delta t\sum_{p=1}^{n}\left(\tilde{\nabla}\mathbf{N}_{pp}^{[i]}\right)^T\frac{\mathbf{k}_p^{t+\Delta t}}{\mu_w}\tilde{\nabla}(p^{t+\Delta t})^{[i]}V_p^{[i]}.\end{aligned}\tag{23}$$

The tangent stiffness matrix for the solid phase, $\mathbf{K}_{C\&S}$, comprises two parts: the material stiffness derived from the algorithmic consistent tangent modulus $\mathbf{C}$ (calculated at the particle level as detailed in Appendix C) and the geometric stiffness $\mathbf{S}$ (see Fang and Yin [51] for the detailed formulation), which is formulated based on the Cauchy total stress here. Consistent with this, the internal force vector $\mathbf{F}_{int}$ is assembled by integrating the updated Cauchy total stresses over the particle volumes. These stress states are strictly updated at the particle level (see Appendix B), ensuring that the calculated internal forces are fully consistent with the material tangent used in the stiffness matrix. A transformation matrix $\boldsymbol{\Gamma}(\cdot)$ is required for the construction of the nonlinear coupling matrix $\mathbf{Q}_{nl}$, which arises from the vector representation of the deformation gradient in Eq. (20). It transforms a 3×1 pressure gradient vector, $\nabla p=[\frac{\partial p}{\partial x},\frac{\partial p}{\partial y},\frac{\partial p}{\partial z}]^T$, into a 3×9 matrix as follows:

$$\boldsymbol{\Gamma}(\nabla p)=\begin{pmatrix}2\frac{\partial p}{\partial x}&\frac{\partial p}{\partial y}&\frac{\partial p}{\partial z}&\frac{\partial p}{\partial y}&0&0&\frac{\partial p}{\partial z}&0&0\\0&\frac{\partial p}{\partial x}&0&\frac{\partial p}{\partial x}&2\frac{\partial p}{\partial y}&\frac{\partial p}{\partial z}&0&\frac{\partial p}{\partial z}&0\\0&0&\frac{\partial p}{\partial x}&0&0&\frac{\partial p}{\partial y}&\frac{\partial p}{\partial x}&\frac{\partial p}{\partial y}&2\frac{\partial p}{\partial z}\end{pmatrix}.\tag{24}$$

2.3. Evolution of hydraulic properties

In large-deformation geomechanics, hydraulic properties, specifically the void ratio (e_p) and hydraulic conductivity (k_p), are fully coupled with the solid matrix deformation [64]. The void ratio is updated based on the volumetric deformation of the particle, which is measured by the determinant of the incremental deformation gradient, $J_p=V_p^{t+\Delta t}/V_p^t$. The void ratio is assumed to be constant within a single time step, so no linearization of this term is required. Based on the relation $J_p=(1+e_p^{t+\Delta t})/(1+e_p^t)$, the update rule is given by:

$$e_p^{t+\Delta t}=J_p(1+e_p^t)-1.\tag{25}$$

The hydraulic conductivity k is typically formulated as a function of the void ratio e. This study adopts two widely used models, the power-law and semi-logarithmic relationships, expressed respectively as:

$$k_p=k_{p0}\left(\frac{e_p}{e_{p0}}\right)^m\quad\text{and}\quad e_p-e_{p0}=C_k\log_{10}\left(\frac{k_p}{k_{p0}}\right),\tag{26}$$

where the subscript 0 denotes initial values, m is a material-dependent empirical exponent, and C_k is the hydraulic conductivity change index.

2.4. Remeshing strategy

To maintain the robustness of the simulation under large deformations, a rigorous mesh quality check is executed at the end of every time step. The quality of each element is evaluated using the aspect ratio metric (defined as the ratio of the shortest to the longest edge). A threshold of 0.3 is adopted; if any element's aspect ratio falls below this value, a two-stage remeshing procedure is triggered.

First, the boundary discretization is optimized using the isotropic explicit remeshing [65] technique. This involves splitting, collapsing, or smoothing boundary edges to generate a high-quality surface representation. Crucially, the positions of these boundary nodes are projected back onto the exact geometry defined by the previous boundary surfaces to minimize volume change. Second, once the boundary is optimized, the interior mesh is completely regenerated (using constrained Delaunay tetrahedralization) based on the new boundary configuration. This ensures that the internal domain is always filled with high-quality isotropic tetrahedra, independent of the previous mesh topology.

2.5. Comparative analysis of computational efficiency and accuracy

To evaluate the performance of the proposed HEPM, we compare its implementation complexity and efficiency with other particle-based methods, specifically the Material Point Method (MPM) and the Particle Finite Element Method (PFEM).

2.5.1. Implementation complexity

From the perspective of implementation complexity, standard methods often require complex modifications to handle large deformation solids effectively. While the original MPM is simple, it suffers from severe cell-crossing noise, quadrature errors and low accuracy [49,66,67]. Although these errors can be mitigated by using higher-order interpolation functions (e.g., B-splines), this approach significantly increases the number of supporting nodes, leading to a significant computational burden in 3D applications.

Adapting PFEM for robust geotechnical analysis introduces specific algorithmic hurdles that are considerably more intricate than those in fluid dynamics [68]. In standard solid PFEM, history variables stored at Gauss points necessitate frequent data mapping to new meshes, leading to inevitable accuracy loss. While Node-Based Smoothed PFEM (NS-PFEM) was proposed to overcome this by storing variables at nodes, it inherently suffers from the overly soft behavior and spurious zero-energy modes due to direct nodal integration [56]. Consequently, establishing a stable formulation (SNS-PFEM) requires introducing complex stabilization terms—such as adding stress points in subdomains. Moreover, a critical limitation in 3D applications is that mesh generation relies entirely on the current positions of physical nodes. The irregular node distribution frequently leads to the generation of "sliver" elements—tetrahedra with nearly coplanar vertices and near-zero volume [53]. These degenerate elements severely compromise the conditioning of the global stiffness matrix, often causing convergence failures in implicit solvers.

In contrast, the proposed HEPM achieves high accuracy and robust stability without relying on complex stabilization algorithms. This is realized through a dual discretization scheme that combines particle-based interpolation reconstruction with the Finite Increment Calculus (FIC) strategy. Crucially, by decoupling the background mesh from the particle-carrying variables, this framework ensures that the mesh is not constrained by the Lagrangian motion of nodes. Consequently, high-quality elements are maintained throughout the analysis.

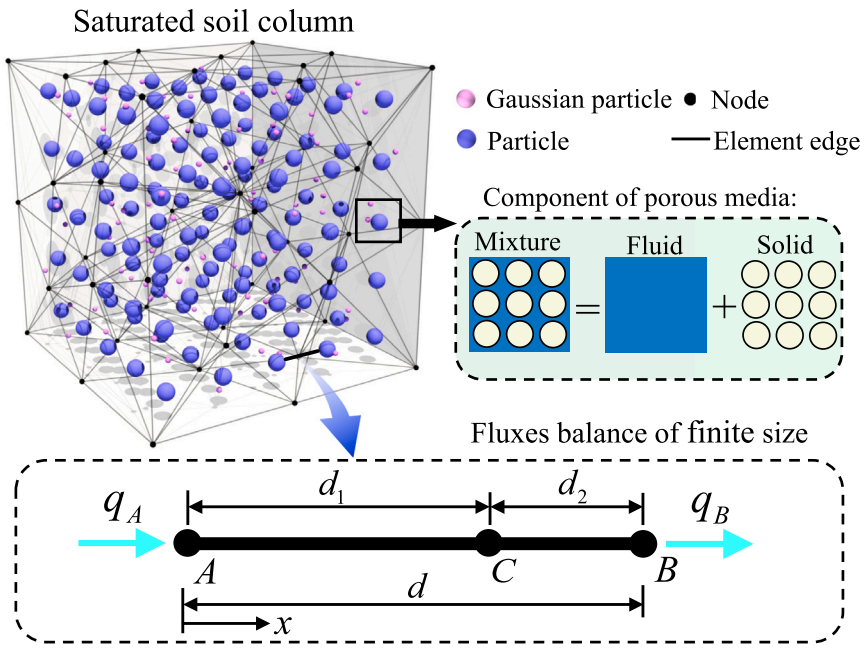

Fig. 2. Schematic representation of the proposed coupling framework. Illustration of the hydro-mechanical coupling for saturated soils and the principle of the particle-based FIC stabilization strategy to suppress pressure oscillations.

2.5.2. Computational efficiency

It is important to acknowledge that no numerical method is universally perfect, and the high accuracy and stability of HEPM come with specific computational costs. Unlike standard FEM which relies on a fixed mesh connectivity, or classic MPM that utilizes a structured background grid, the proposed HEPM adopts a dual discretization scheme. This introduces additional algorithmic treatments, primarily the neighbor search and the reconstruction of interpolation functions at every time step. Consequently, for a simulation with the same number of degrees of freedom, the computational cost per time step in HEPM is inevitably higher than that of standard FEM or the original MPM.

However, when compared to advanced node-based methods designed for similar large-deformation accuracy, such as the SNS-PFEM, HEPM demonstrates a competitive efficiency profile. SNS-PFEM necessitates a computationally expensive loop over node neighbors to perform strain smoothing integration. More critically, to suppress zero-energy modes, it requires complex stabilization schemes involving geometric sub-domain operations [56]. In contrast, HEPM achieves stability through the simple FIC formulation, thereby avoiding these time-consuming stabilization calculations. A detailed quantitative comparison of computational time between HEPM and SNS-PFEM has been reported in our previous study [51], which verified that HEPM offers a favorable balance between accuracy and cost.

3. Particle-based FIC stabilized method

The Finite Increment Calculus (FIC) method is applied to stabilize the pressure field of particles in the proposed FIC-stabilized HEPM. This method begins by expressing the governing differential equation in its residual form, $r_p = 0$, by incorporating higher-order terms derived from a Taylor series expansion of the residual over a finite domain with length d (Fig. 2). Based on a formulation that includes higher-order differential terms [62], the resulting stabilized residual equation with the use of low order elements, simplified for a low-permeability condition, is expressed as:

$$r_p = (\mathbf{Q}_P^T + \Delta t\mathbf{Q}_{nl})\Delta\mathbf{u} + (\mathbf{T}_P^{stab} + \Delta t\mathbf{H}_P)\Delta\mathbf{p} - \mathbf{R}_P^{stab} = 0, \tag{27}$$

where the term $\mathbf{R}_P^{stab}$ represents the stabilized residual vector from Eq. (23), and $\mathbf{T}_P^{stab}$ is the stabilization matrix. They are explicitly defined as:

$$\begin{aligned}\mathbf{R}_P^{stab} &= \Delta t\mathbf{F}_P - \mathbf{F}_Q - \mathbf{F}_H - \mathbf{T}_P^{stab}(\mathbf{p}^{t+\Delta t} - \mathbf{p}^t),\\ \mathbf{T}_P^{stab} &= \sum_{p=1}^{n}(\tilde{\nabla}\mathbf{N}_{pp})^T(\tilde{\nabla}\mathbf{N}_{pp})(\tau\alpha)V_p,\end{aligned} \tag{28}$$

where the stabilization parameter is defined as $\tau = h^2\alpha/(8G)$, with $h = \sqrt[3]{6V_p/\pi}$ representing the characteristic length of an equivalent sphere for a particle with volume V_p and shear modulus G. Thus, after incorporating the stabilization term, the particle-based discrete form of the mass conservation equation (Eq. (22)) becomes:

$$[(\mathbf{Q}_P^{[i]})^T + \Delta t\mathbf{Q}_{nl}^{[i]}]\Delta\mathbf{u}^{[i]} + (\mathbf{T}_P^{stab} + \Delta t\mathbf{H}_P^{[i]})\Delta\mathbf{p}^{[i]} = (\mathbf{R}_P^{stab})^{[i]}. \tag{29}$$

4. Numerical verification and benchmarking

This section presents several numerical examples to verify and demonstrate the performance of the proposed FIC-stabilized HEPM in consolidation analysis. Initially, several small deformation problems serve to verify the fundamental accuracy and spatial convergence against analytical solutions and to investigate the efficacy of the implemented pressure stabilization technique. Subsequent examples are intended to demonstrate the capability of the proposed method for simulating large-deformation nonlinear consolidation. Finally, two case studies of severe mesh distortion are used to showcase the method's advantages in handling problems that pose a significant challenge to traditional mesh-based approaches.

4.1. Surface loading of an elastic soil foundation

This section systematically evaluates the pressure stabilization of the proposed method by analyzing a classic three-dimensional foundation consolidation problem. The performance in terms of accuracy and stability is assessed by benchmarking its predictions of pore pressure distribution against results from the standard FEM [69]. The geometry and boundary conditions of the three-dimensional model are depicted in Fig. 3. Two distinct meshing strategies and fully undrained conditions are considered. Specifically, Fig. 3a shows the dimensions and boundary conditions of the model. Fig. 3b illustrates the two mesh

configurations considered in this study: a uniform coarse mesh and a locally refined mesh. The uniform and refined meshes, with 8283 and 10,264 elements respectively, are slightly less discretized than their counterparts in Ref. [69] (which featured 9985 and 13,532 elements, respectively). The corresponding particle distributions for each meshing strategy are shown in Fig. 3c. The material properties are set as follows: Young's modulus $E = 25$ MPa, Poisson's ratio $\nu = 0.2$, and fluid viscosity $\mu = 1 \times 10^{-3}$ Pa s. The hydraulic conductivity is set to $k_w \approx 1\times10^{-7}$ m/s and all other parameters are kept consistent with reference. A uniformly distributed pressure of $P_{surf} = 10$ kPa is applied to a portion of the top surface. The four lateral boundaries are constrained against normal displacement to simulate a confined soil column, while the bottom boundary is fully fixed. The simulation is run for a total duration of 1 s.

The simulation results, presented in Fig. 4, clearly illustrate the maximum pressure evolution in HEPM and FEM. For the case with a uniform coarse mesh, the initial maximum pore pressure computed by HEPM is significantly closer to the applied surface pressure than that obtained from FEM, under undrained conditions. This indicates that HEPM maintains a higher degree of computational accuracy and exhibits superior convergence properties even with a low-density mesh (Fig. 4a). When a locally refined mesh is employed, the accuracy of both methods improves significantly. The numerical solutions from both HEPM and FEM demonstrate excellent agreement, which validates the effectiveness of both approaches on a sufficiently refined mesh (Fig. 4b).

Furthermore, the necessity and efficacy of the pressure stabilization technique are visually confirmed in Fig. 5. Without stabilization, the pressure field computed on the uniform coarse mesh exhibits severe, non-physical oscillations and negative pressure values (Fig. 5a). Similarly, for the locally refined mesh, the unstabilized solution exhibits a pronounced checkerboard pattern of pressure oscillations (Fig. 5b). In contrast, the application of the particle-based FIC method effectively eliminates these numerical instabilities in both cases, yielding a smooth, stable, and physically realistic pore pressure distribution. This result strongly demonstrates that the FIC-stabilized HEPM can effectively overcome the numerical instabilities that may arise in the FEM for such problems, thereby providing more reliable and accurate simulation predictions.

4.2. One-dimensional consolidation

This section assesses the accuracy of pressure evolution and investigates the spatial convergence of the proposed FIC-stabilized HEPM by analyzing the one-dimensional (1D) consolidation problem based on Terzaghi's consolidation theory. The setup for the 1D consolidation model is depicted in Fig. 6a. The boundary conditions include a surface pressure of $P_{\text{surf}} = 1$ kPa applied to the top. Regarding the hydraulic conditions, the top surface is treated as a fully drained boundary, while the lateral and bottom boundaries are assumed to be impermeable. The lateral boundaries are constrained against normal displacement, while the bottom boundary is constrained against vertical displacement. In this model, the problem domain with $H = 1$ m is discretized by particles, while the mesh serves as an auxiliary tool primarily for the application of boundary conditions. An elastic constitutive model is adopted for the material. The parameters are set as follows: Young's modulus $E = 100$ MPa, Poisson's ratio $\nu = 0.2$, porosity $n = 0.2$, the unit weight of water $\gamma_w = 9.81$ kN/m^3 and hydraulic conductivity $k_w = 9\times10^{-3}$ m/s. The analytical solution for this problem is given by:

$$p(t,z) = \frac{4P_{surf}}{\pi}\sum_{n=0}^{\infty}\frac{1}{2n+1}\sin\left(\frac{(2n+1)\pi z}{2H}\right) \times \exp(-(n+1/2)^2\pi^2 T),\ \text{with } T = k_w t/(\gamma_w m_v H^2), \tag{30}$$

where t is the elapsed time since the load application and z is the vertical coordinate measured from the top drainage boundary; m_v represents the coefficient of compressibility and T is the dimensionless time factor. Fig. 6b presents a comparison between the pore pressure distribution obtained from HEPM and Terzaghi's analytical solution, showing perfect agreement at $T = 0.001, 0.01, 0.05, 0.1, 0.2, 0.5, 1.0$. As illustrated in the convergence analysis in Fig. 6c, both the conventional Updated Lagrangian FEM (UL-FEM) and HEPM methods exhibit a convergence rate approaching the second order with mesh refinement. A quantitative analysis of the error decay reveals that the proposed HEPM consistently achieves a super-quadratic convergence rate of 2.39, which is significantly higher than the nearly quadratic rate of 1.92 obtained for the UL-FEM. This superior convergence property underscores the computational efficiency of HEPM, indicating that a desired level of accuracy can be achieved with a coarser mesh and, consequently, less computational effort compared to the UL-FEM.

Furthermore, the global mass conservation of the proposed framework is rigorously verified through the 1D consolidation benchmark. In a fully saturated system, the reduction in the solid skeleton volume (ΔV_s) must be balanced by the cumulative volume of fluid expelled from the domain (V_f), as compared in Fig. 7. The fluid outflow matches the solid compression with exceptional precision. The normalized error, defined as $|\Delta V_s - V_f|/V_0$, where V_0 denotes the initial total volume of the soil column, remains on the order of 10^{-6} at the end of the consolidation process. This negligible discrepancy, primarily attributed to minor numerical integration errors, confirms that the proposed algorithm strictly satisfies the principle of mass conservation.

4.3. One-dimensional two-layered consolidation

This section validates the proposed method against an analytical solution for the 1D consolidation of a two-layered soil column. The simulation is designed to assess the method's ability to handle material heterogeneity and mitigate spurious pore pressure oscillations at small initial time steps. As illustrated in Fig. 8a, a parametric study is performed by varying the ratio of layer height ($c = h_1/h_2$: 1, 4/6, 3/7, 2/8) and the ratio of hydraulic conductivity ($a = k_1/k_2$: 0.25, 4). The model setup replicates the analytical conditions: a 1D strain state is enforced by applying a uniform pressure to the top surface, fixing the base, and constraining lateral boundaries. Consistent with the analytical solution, the top surface is allowed to drain freely, whereas the base and lateral sides are set as impermeable boundaries. To match the analytical solution, the soil is modeled as an elastic material with a Young's modulus of 6 MPa, and the domain is discretized using 5653 particles and a mesh with a characteristic size of 0.02 m.

Based on Terzaghi's theory, Xie et al. [70] provides an analytical solution for one-dimensional consolidation in a two-layered soil. The excess pore water pressure in each layer is expressed as an infinite series:

$$u_1 = q_0\sum_{m=1}^{\infty}C_m\left[\sin\left(\frac{\lambda_m}{H}z\right) + \frac{\lambda_m}{R_1}\cos\left(\frac{\lambda_m}{H}z\right)\right]\exp(-\lambda_m^2 T_{v1}), \tag{31}$$

$$u_2 = q_0\sum_{m=1}^{\infty}C_m W_m\left[\mu\lambda_m\cos\left(\mu\lambda_m\frac{H-z}{H}\right) + R_2\sin\left(\mu\lambda_m\frac{H-z}{H}\right)\right]\exp(-\lambda_m^2 T_{v1}), \tag{32}$$

where u_1, u_2 are the excess pore water pressures in clay layer 1 and clay layer 2, respectively; q_0 is the continuous uniform loading applied on the top surface; T_{v1} is the dimensionless time factor for upper layer, defined as $c_{v1}t/H^2$. More details can be found in Xie et al. [70].

As illustrated in Fig. 8b and d, when the upper layer is more permeable, its pore pressure dissipates rapidly towards a linear distribution, while dissipation in the lower, less permeable layer is significantly slower. As the upper layer's relative thickness decreases (a smaller c value), the slow drainage from the bottom layer increasingly governs the overall consolidation rate. Conversely, when the lower layer is more permeable (Fig. 8c and e), it dissipates pore pressure uniformly

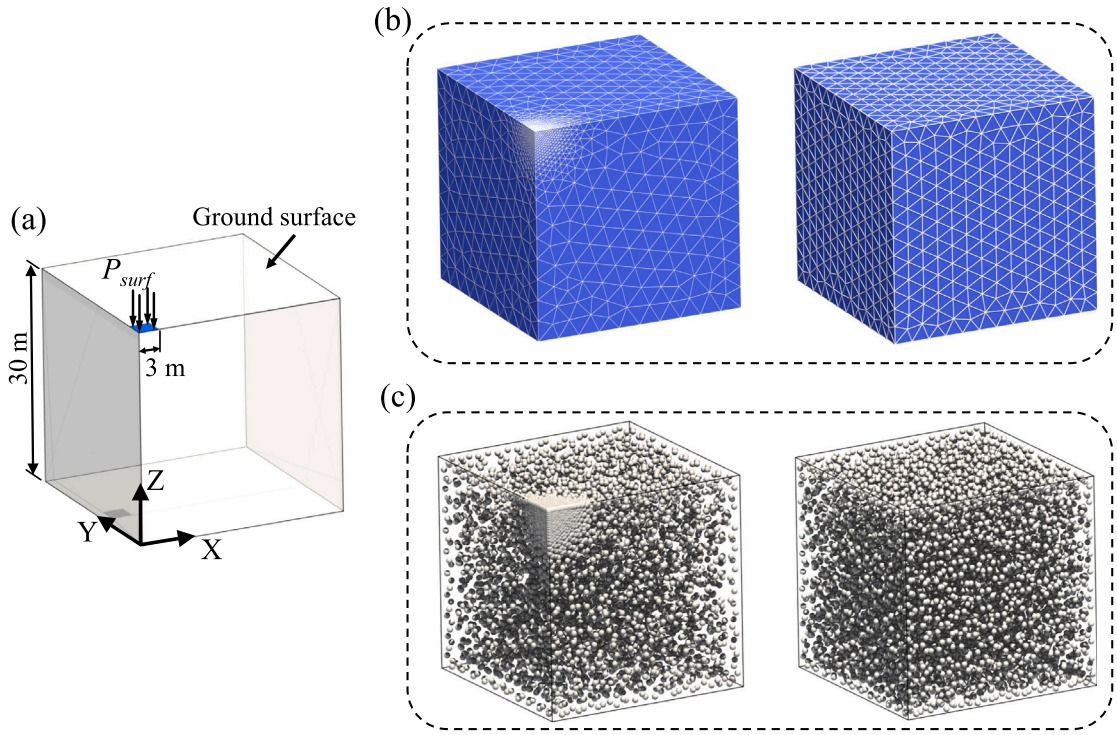

Fig. 3. Numerical model and discretization scheme for the 3D footing consolidation problem. (a) 3D computational domain with surface loading P_{surf}. (b) Background mesh showing non-uniform refinement (left) and uniform discretization (right). (c) Associated particle distributions generated based on the mesh size.

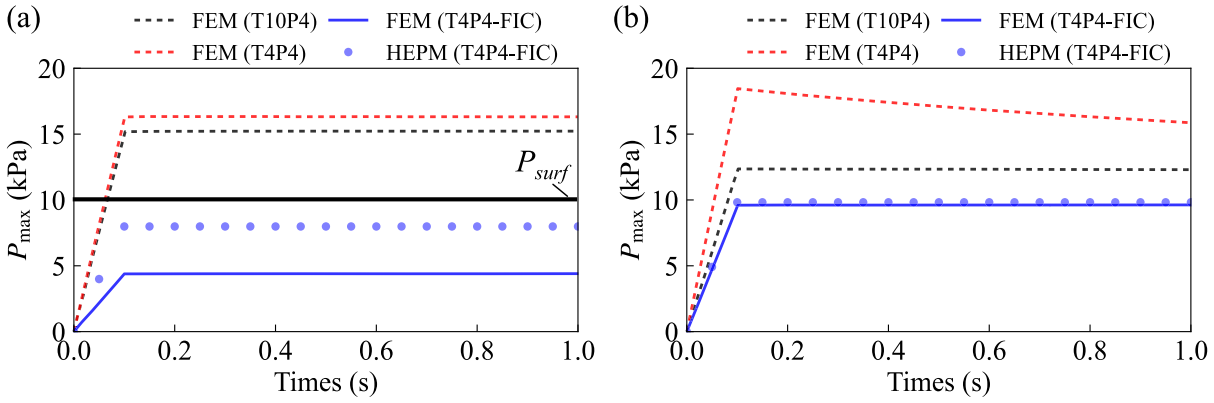

Fig. 4. Evolution of maximum pore pressure under undrained conditions in the surface loading test. (a) Results with a uniform mesh. (b) Results with a locally refined mesh. The plots compare the proposed FIC-stabilized HEPM against reference FEM: standard low-order (T4P4), high-order (T10P4), and FIC-stabilized FEM.

across its depth. Consequently, the less permeable upper layer dictates the overall dissipation process. Fig. 9 compares pore pressure distributions from different stabilization strategies to evaluate the performance of FIC-stabilized HEPM in mitigating oscillations. The stabilization analysis adopts a low hydraulic conductivity ($k = 10^{-6}$ m/s) and a small initial time step ($T_{v1} = 1 \times 10^{-5}$) to provoke instability. Without any stabilization, severe non-uniform oscillations appear in both nodes and particles near the top surface. The Polynomial Pressure Projection (PPP) strategy significantly improves stability, confining over-pressurization—where pore pressure exceeds the applied load—to localized regions and eliminating oscillations at depth. By contrast, the proposed FIC method yields a superior result, producing an even more stable pressure field and further reducing the magnitude of over-pressurization. These results confirm that the FIC-stabilized HEPM effectively suppresses spurious pressure oscillations, ensuring a robust and stable foundation for subsequent consolidation analysis.

4.4. Cryer's sphere with Mandel–Cryer effect

A key feature of 3D consolidation is the transfer of total stress during drainage. This mechanism can cause the excess pore pressure at interior points to temporarily exceed its initial value, a phenomenon known as the Mandel–Cryer effect. The classic Cryer's sphere consolidation problem [71] is simulated in this section and the corresponding analytical solution for pore pressure dissipation and the time-dependent volumetric response are expressed as follows:

$$\begin{aligned} \frac{P}{P_0} &= \sum_{n=1}^{\infty} \frac{-8\mu + 2(4\mu - s_n)/\cos\sqrt{s_n}}{s_n - 12\mu + 16\mu^2} \exp(-s_n T), \\ \frac{\Delta V}{V_0} &= \frac{-P}{S + 2N/3} \left[1 - 2 \sum_{n=1}^{\infty} \frac{3 - 4\mu}{s_n - 12\mu + 16\mu^2} \exp(-s_n T) \right]. \end{aligned} \tag{33}$$

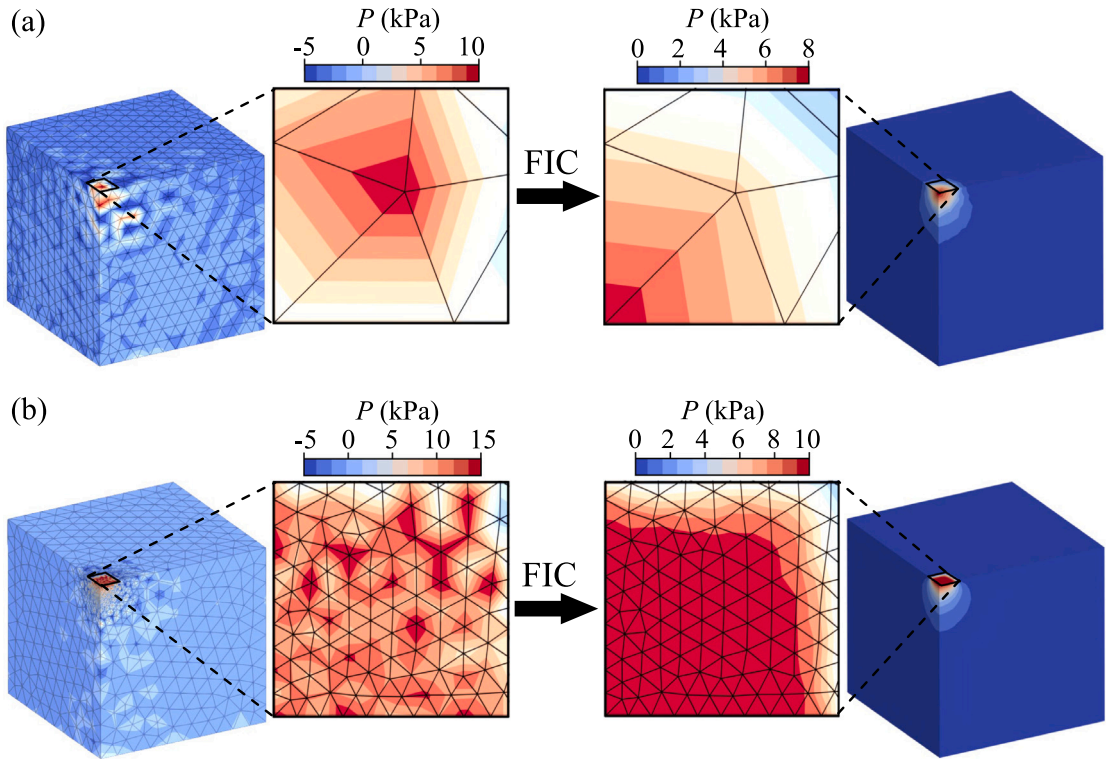

Fig. 5. Comparison of pore pressure contours illustrating the effect of FIC stabilization in the surface loading test. (a) Case with uniform coarse mesh. (b) Case with locally refined mesh. The solution obtained by the standard low-order formulation is presented on the left, while the result from the proposed FIC-stabilized algorithm is shown on the right.

where T is the dimensionless time factor; P is the pore pressure at sphere center; the term $\Delta V/V_0$ is the average volumetric strain of the sphere with an initial volume V_0, a is the radius of the sphere; More details can be found in Cryer [71]. As shown in Fig. 10, a 1/8 spherical sector is analyzed by virtue of symmetry, with a uniform surface pressure of $P_{surf} = 5$ kPa applied to simulate a hydrostatic load. The domain's discretization involves a mesh size of 0.05 m, resulting in approximately 2600 particles. The mechanical behavior of the soil is characterized by a linear elastic model with a Young's modulus E of 1 MPa. The analysis investigates the influence of the Mandel–Cryer effect by considering three Poisson's ratios ν: 0.0, 0.2, and 0.4. The hydraulic properties are defined by a hydraulic conductivity $k = 10^{-5}$ m/s and a fluid viscosity of 1.0×10^{-3} Pa s.

As illustrated in Fig. 11, the evolution of both the pore pressure and volume change at sphere center shows excellent agreement with the analytical solution. Notably, the simulation successfully captures the Mandel–Cryer effect, which is characterized by an initial rise in excess pore pressure followed by its eventual dissipation. Furthermore, the results indicate that this effect becomes more pronounced for smaller values of Poisson's ratio, which correspond to larger volumetric changes in the solid skeleton.

To validate the performance in stabilizing 3D pore pressure distribution, the results from different stabilization strategies are compared. The simulation adopts a small $k = 1 \times 10^{-6}$ m/s and $T_{v1} = 1 \times 10^{-6}$ to provoke instability. The pore pressure distribution is examined along radial lines at various polar angles throughout the sphere. From these multiple profiles, we generate an envelope plot that delineates the maximum and minimum pore pressure values recorded at each radial distance r. This envelope serves as a visual indicator of numerical stability: a wider envelope implies significant oscillations in pressure values across different angles, whereas a narrower envelope indicates a smoother, more uniform pressure field. The numerical results for three strategies are presented in Fig. 11c: Case 1 for unstabilized condition, Case 2 for PPP method with commonly used penalization term [56], and Case 3 for FIC method. The unstabilized Case 1 exhibits severe pressure concentrations with a large envelope width ($L_{max} = 4.3$ kPa). In contrast, both stabilized cases effectively suppress these oscillations. Notably, the proposed Case 3 achieves the narrowest envelope ($L_{max} = 1.8$ kPa) compared to Case 2 ($L_{max} = 2.8$ kPa), demonstrating the superior stability of the FIC formulation.

4.5. Gibson's consolidation with large deformation

In this section, the numerical results are compared with the analytical solutions for 1D large-strain consolidation presented by Xie and Leo [72]. A key finding from this theory is that large-strain analysis predicts a smaller total settlement but a faster consolidation rate for both settlement development and excess pore pressure dissipation compared to classical small-strain theory. This distinction is critical for understanding the behavior of soft ground undergoing large deformation. For a pervious top and an impermeable bottom boundary, the analytical solutions for excess pore water pressure and the average degree of consolidation are as follows: The excess pore pressure u is given by:

$$u = \frac{1}{m_v} \ln \left\{ 1 + \left[\exp(m_v q_u) - 1 \right] \sum_{m=1}^{\infty} \frac{2}{M} \sin\left(\frac{Ma}{H}\right) \exp(-M^2 T_v) \right\}, \quad (34)$$

where q_u is the applied surface load, m_v is the volume compressibility for large strain (ε), a is the Lagrangian coordinate, H is the initial thickness of the clay layer, and T_v is the dimensionless time factor, defined as $T_v = c_v t/H^2$. The term M is defined as $M = (m - 1/2)\pi$ for $m = 1, 2, 3, \ldots$. In large-strain theory, the average degree of consolidation can be defined by stress (U_p) or by strain (U_s), and the two are not identical. U_s is adopted, representing the normalized settlement S_t/S_∞,

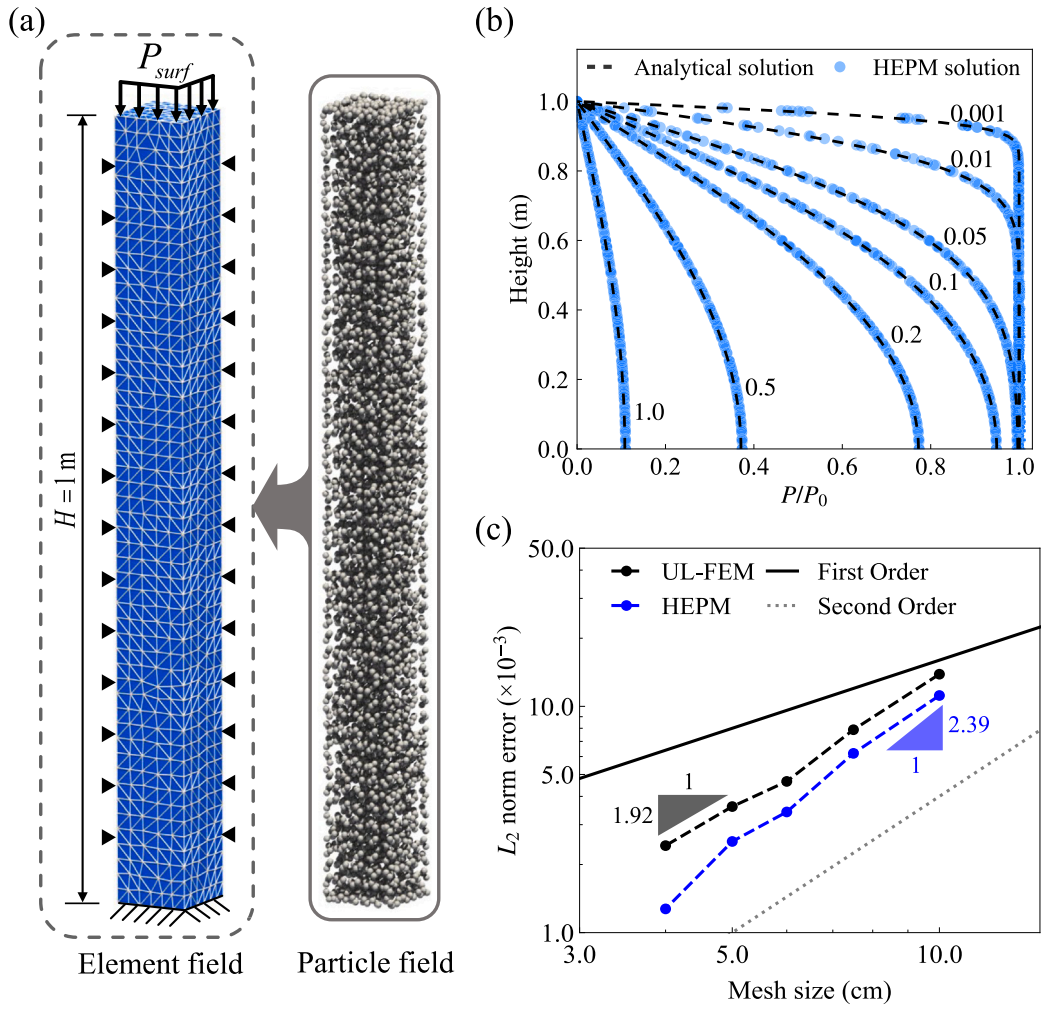

Fig. 6. Verification of the coupled hydro-mechanical model using a 1D consolidation test. (a) Schematic of the soil column setup, including mesh and boundary conditions. (b) Comparison of the pore pressure evolution against Terzaghi's analytical solution. (c) Spatial convergence analysis.

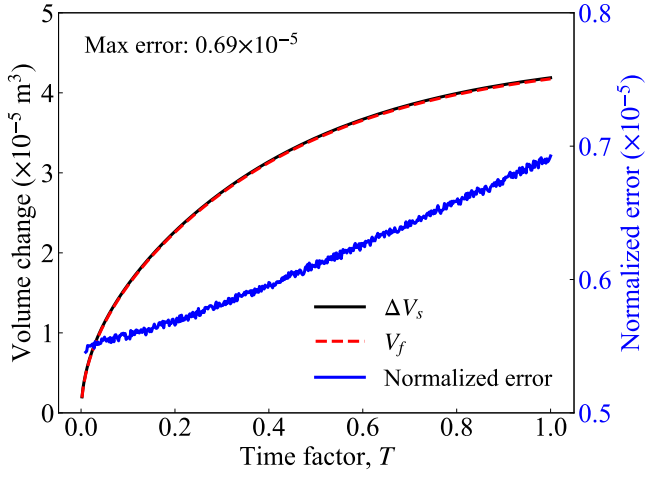

Fig. 7. Verification of mass conservation for the 1D consolidation problem. The comparison between soil skeleton compression (ΔV_s) and fluid outflow (V_f) is presented on the left axis, while the evolution of the normalized error is shown on the right axis.

where the final settlement is $S_\infty = H[1 - \exp(-m_v q_u)]$. The explicit solution is:

$$U_s = \frac{S_t}{S_\infty} = 1 - \sum_{m=1}^{\infty} \frac{2}{M^2} \exp(-M^2 T_v). \tag{35}$$

The differences in settlement behavior between large-strain and small-strain consolidation theories are investigated through a parametric study. The material properties are held constant, with a Young's modulus of $E = 1.0 \times 10^6$ Pa and a Poisson's ratio of $\nu = 0.2$. In the analytical solution, the term m_v is the inverse of the bulk modulus, given by the formula $(1 + \nu)(1 - 2\nu)/[E(1 - \nu)]$. The analysis considers three compressibility-load ratios ($\lambda_m = m_v q_u$): 0.09, 0.18, 0.27. These ratios correspond to surface pressures of 100 kPa, 200 kPa, and 300 kPa, respectively. The boundary conditions are identical to those in the 1D consolidation case described previously. As shown in Fig. 12a, the pore pressure distribution at various degrees of consolidation show excellent agreement with the analytical solution. As shown in Fig. 12b, the evolution of the degree of consolidation for different values of λ_m demonstrates excellent agreement with the large-strain analytical solution. The comparison also highlights the importance of the large-strain formulation. While the discrepancy between the large- and small-strain solutions is minor for a low λ_m of 0.09, this difference becomes more pronounced as λ_m increases. Notably, for the case of $\lambda_m = 0.27$, the analysis predicts a final settlement of 0.24 m, showcasing a significant deviation from the small-strain prediction.

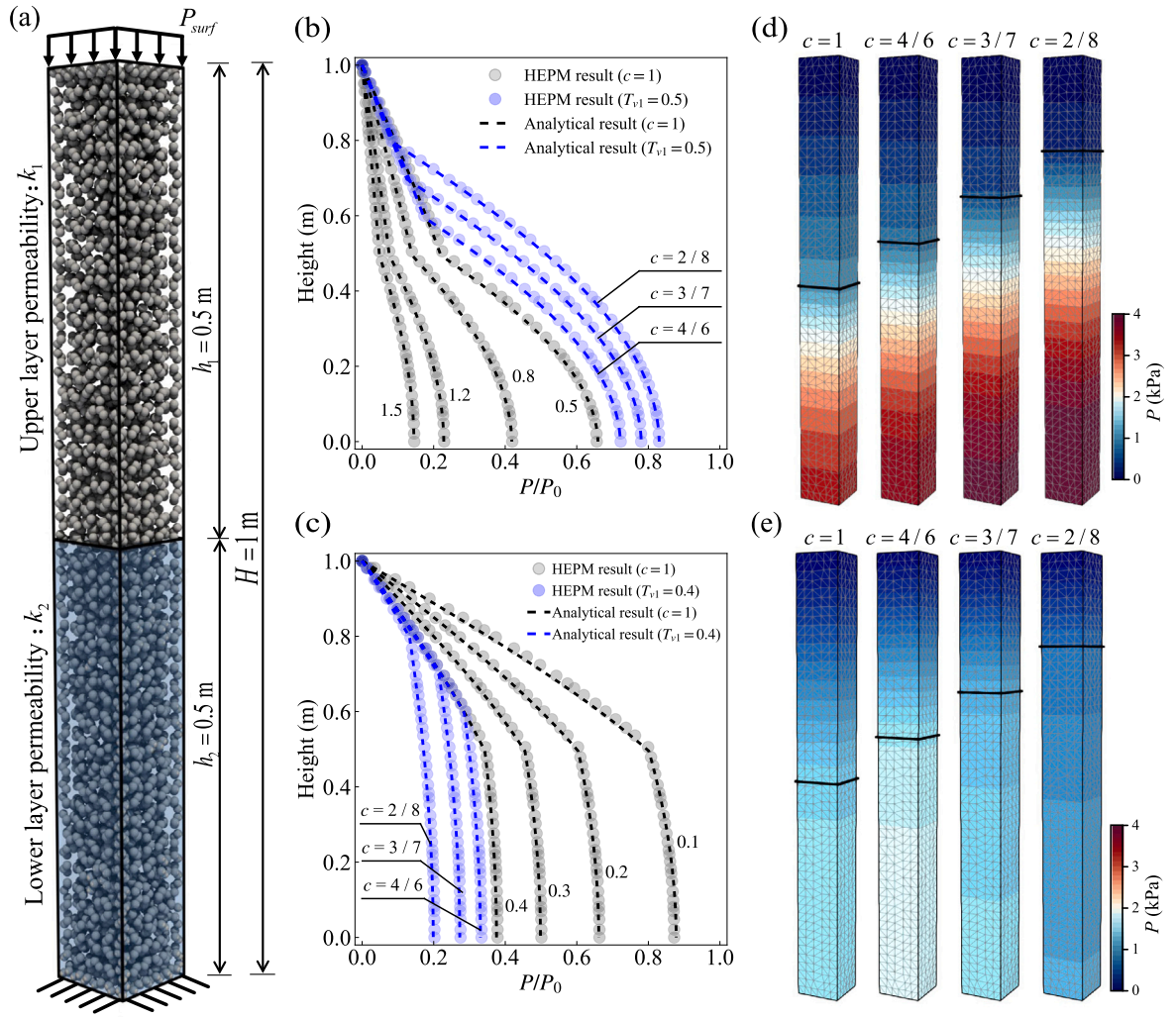

Fig. 8. Verification of the coupled hydro-mechanical model using a 1D two-layered consolidation test. (a) Schematic of the model setup, defining the two soil layers and boundary conditions. (b-c) Comparison of simulated pore pressure distributions against the analytical solution for two different permeability ratios, $a = 0.25$ and $a = 4$. (d-e) Corresponding pore pressure contours.

This demonstrates the accuracy and reliability of the FIC-stabilized HEPM in simulating large-deformation consolidation.

To rigorously verify that the frequent spatial discretization changes induced by the remeshing strategy do not compromise numerical accuracy or solver convergence, a quantitative assessment was conducted using the large-strain consolidation benchmark (axial strain > 15%). Since the deformation in this controlled case does not induce element distortion, a direct comparison was made between the simulation with frequent remeshing enabled (U_{Remesh}) and the simulation without remeshing (U_{Fixed}) to isolate the effects of the remeshing operation. Fig. 13a presents the comparison of settlement evolution, which is virtually identical. The accuracy is further quantified in Fig. 13b by the relative error, defined as $\varepsilon = |U_{Remesh} - U_{Fixed}|/|U_{Fixed}| \times 100\%$. The results indicate that the error introduced by the remeshing procedure is negligible, with the relative error converging to a stable value of 0.027%. This confirms that the proposed algorithms strictly preserve the solution precision. It is important to note that this minor difference is not solely attributable to remeshing. In numerical analysis, different mesh configurations—even with the same global element size—naturally yield marginally different results.

To evaluate the impact on algorithmic efficiency, we monitored the number of iterations per time step N_{iter} required for convergence at representative time steps. As illustrated in Table 1, the no remeshing case generally requires fewer iterations compared to the remeshing case. This slight difference is expected, as the frequent changes in spatial discretization inevitably introduce minute numerical perturbations, which require the solver to perform slight re-equilibration. However, this minor computational cost is a reasonable trade-off for the capability to robustly simulate extreme mesh distortions.

Table 1
Comparison of the number of iterations per time step (N_{iter}) required for convergence at selected time steps for cases with and without remeshing.

Time factor (T)	Iterations (N_{iter})	
	Without remeshing	With remeshing
0.05	4	5
1.0	3	4
3.0	2	3

4.6. Cryer's sphere with variable hydraulic conductivity

This section presents a three-dimensional consolidation simulation that incorporates large deformations. In large-strain consolidation, the hydraulic properties of the soil skeleton change significantly with deformation. This behavior introduces a strong nonlinearity that has a dominant influence on the consolidation process. To investigate this,

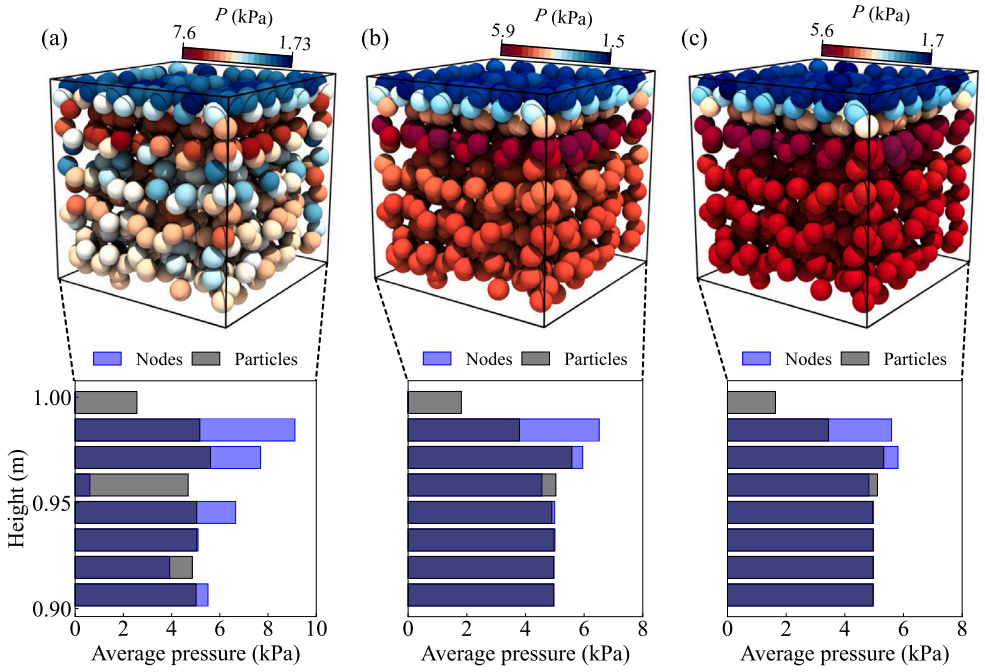

Fig. 9. Comparison of pore pressure distributions in 1D consolidation predicted by different stabilization methods. The results are shown for a dimensionless time factor of $T = 1 \times 10^{-5}$ with $k = 1 \times 10^{-6}$ m/s. (a) Standard formulation without stabilization. (b) Polynomial Pressure Projection (PPP) method. (c) Finite Increment Calculus (FIC) method.

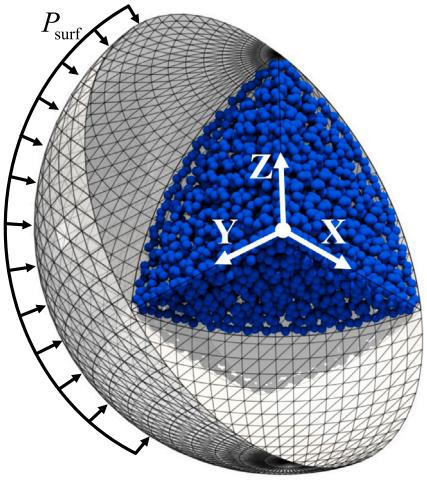

Fig. 10. Computational model for the Cryer's sphere consolidation problem (1/8 symmetric domain). The external surface is subjected to a constant load P_{surf} under fully drained conditions, while the symmetry planes are constrained by symmetry rollers.

we analyze the consolidation of a three-dimensional sphere under large deformation, focusing on the effects of different void-ratio dependent hydraulic conductivity relationships. Since an explicit analytical solution for this nonlinear problem is generally unavailable, numerical methods are typically required. For validation, we refer to the numerical solution presented by Gibson et al. [73]. The governing equation derived in their work, expressed in the material coordinate ξ, is given as:

$$\frac{\partial^2 \xi}{\partial a^2} + \frac{2\nu}{(1-\nu)} \frac{1}{\xi} \frac{\partial \xi}{\partial a} \left[\frac{\partial \xi}{\partial a} - \frac{\xi}{a} \right] + 2 \left(\frac{1-2\nu}{1-\nu} \right) \frac{1}{\xi} \left(\frac{\partial \xi}{\partial a} \right)^2 \ln \left[\frac{a}{\xi} \frac{\partial \xi}{\partial a} \right] = \frac{1}{c_v} \left(\frac{\partial \xi}{\partial a} \right)^2 \frac{\partial \xi}{\partial t}. \tag{36}$$

Once the solution for $\xi(a,t)$ is obtained, the excess pore water pressure, P, can be calculated by the following integral:

$$P(a,t) = \int_{a_0}^{a} \frac{\gamma_w}{k} \frac{\partial \xi}{\partial a'} \frac{\partial \xi}{\partial t} da', \tag{37}$$

where ξ is the current radius of a material point at time t with an initial radius of a; The material properties include the Poisson ratio of the soil skeleton, ν, and the hydraulic conductivity, k, which may depend on the void ratio. The analysis focuses on the evolution of the pore pressure at the center of the sphere, denoted as $P(0,T)$. This pressure is expressed as a function of the dimensionless time factor, $T = \frac{c_v t}{a_0^2}$, and the parameter c_v is the coefficient of consolidation, defined as $c_v = \frac{kE(1-\nu)}{\gamma_w(1+\nu)(1-2\nu)}$, where γ_w is the unit weight of the pore water. The material parameters and nonlinear hydraulic conductivity functions adopted in this model, are listed in Table 2. These models characterize the hydraulic conductivity behavior of copper tailings using a semi-logarithmic relationship (SS1) and Florida phosphatic clay using a power-law relationship (SS2). All other boundary conditions are consistent with the small-strain Cryer's problem.

As shown in Fig. 14, the results obtained from the proposed HEPM are in excellent agreement with the finite difference solution. It is observed that when nonlinear hydraulic parameters are considered, the dissipation of pore water pressure becomes significantly slower compared to the constant parameter case. Furthermore, this retardation effect is more pronounced as the stiffness ratio λ increases (e.g., at $\lambda = 0.1$ and 0.25), leading to a greater deviation from the linear consolidation curve. Fig. 15 illustrates the particle pore pressure at $T = 1$, showing a smooth pressure distribution throughout the particle domain under all tested conditions. Notably, the results also show that for the same λ_m value, the choice of hydraulic conductivity relationship leads to significant differences in the resulting surface settlement. These findings demonstrate that the FIC-stabilized HEPM not only shows excellent agreement with reference solutions but also accurately captures the complex effects of material nonlinearity on both pore pressure dissipation and surface settlement, all while maintaining a stable and uniform pressure field.

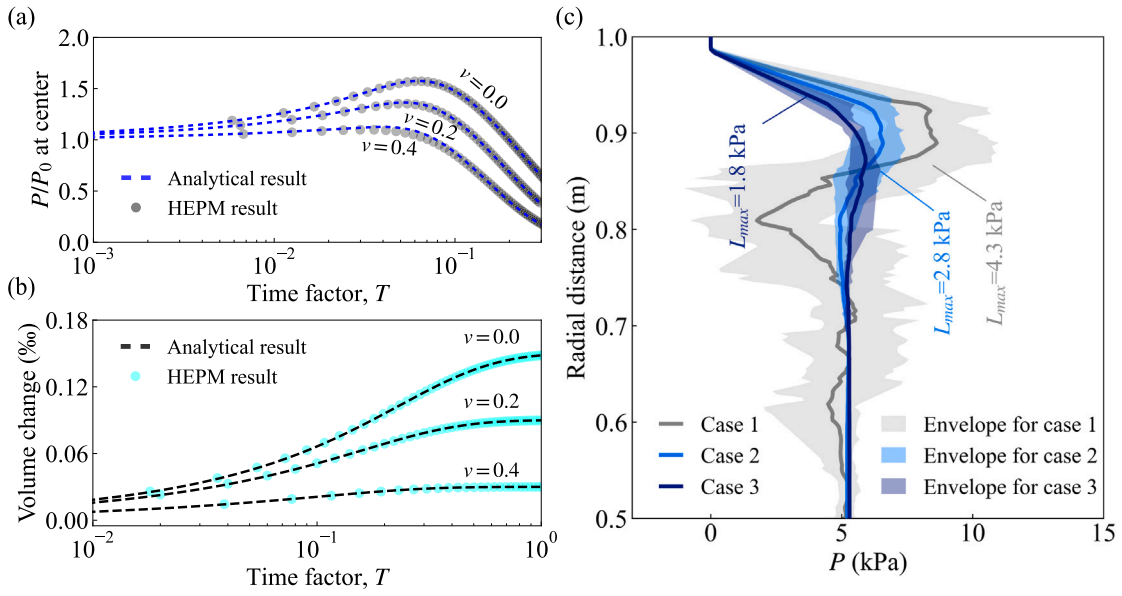

Fig. 11. Comparison of HEPM results of the Cryer's sphere consolidation with analytical solutions for varying Poisson's ratios. (a) Pore pressure at the sphere center. (b) Overall volume change. (c) Envelopes of radial pressure profiles of different pressure stabilization methods at T = 0.0001.

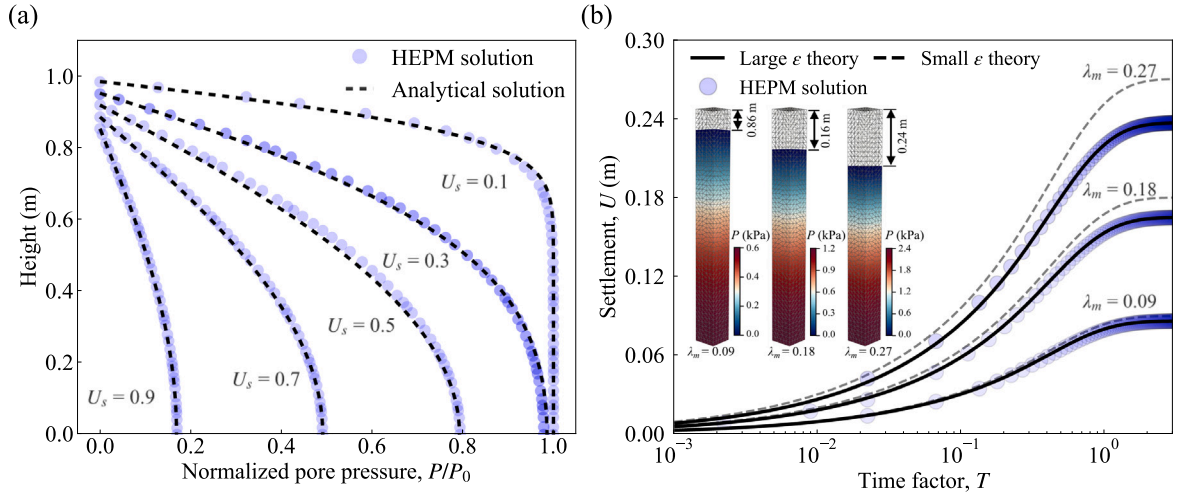

Fig. 12. Comparison between analytical solutions and results from the proposed HEPM in 1D large-strain consolidation. (a) Normalized pore pressure for different values of U_s. (b) Average degree of consolidation (%) with different values of λ_m.

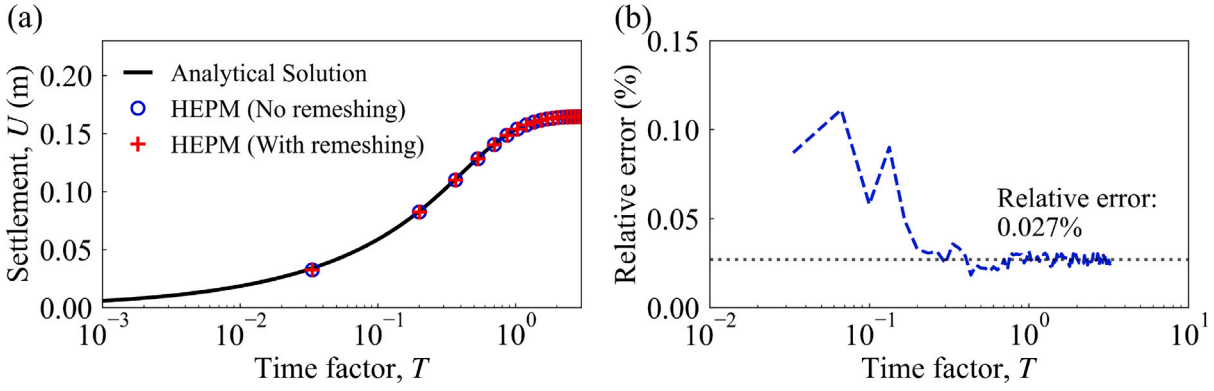

Fig. 13. Quantitative verification of the remeshing consistency in 1D large-strain consolidation. (a) Comparison of settlement between the proposed HEPM with frequent remeshing and HEPM without remeshing. (b) Evolution of the relative error over time.

Table 2
Comparison of material properties for the two soils.

Property	Copper tailings	Florida phosphatic clay
Young's modulus, E	1.0 MPa	
Poisson's ratio, ν	0.0	
Hydraulic conductivity, k_0	1.0×10^{-4} m/s	
Initial void ratio, e_0	1.42	4.00
Hydraulic conductivity model	$k = k_0 \exp[4.11(e - e_0)]$ (SS1)	$k = k_0(e/e_0)^{4.11}$ (SS2)

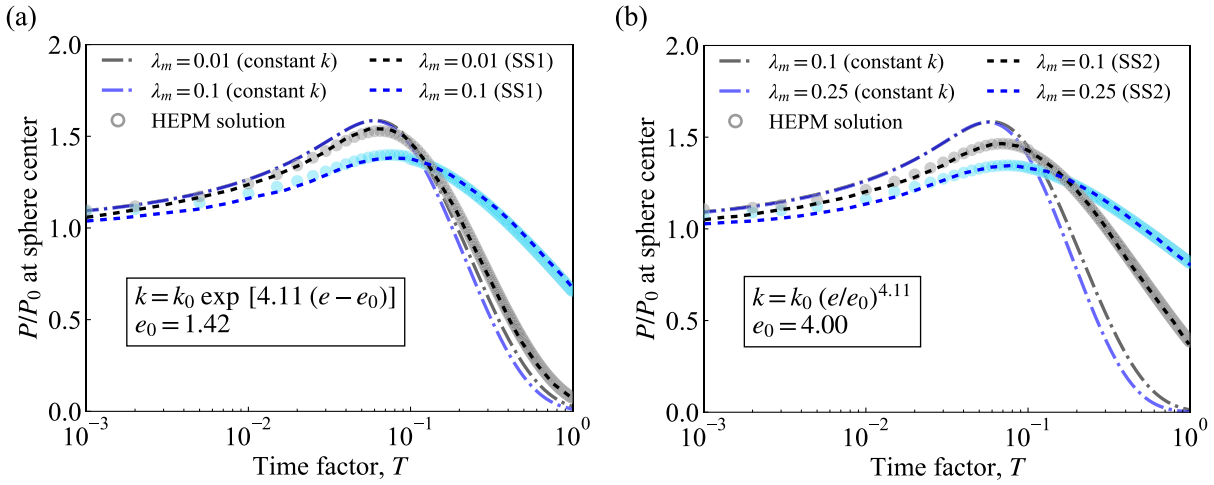

Fig. 14. Evolution of normalized pore pressure P/P_0 at the center of Cryer's sphere for different λ_m values. (a) Exponential model. (b) Power-law model. The plots contrast the solutions obtained under the assumption of constant permeability against those considering void ratio-dependent permeability.

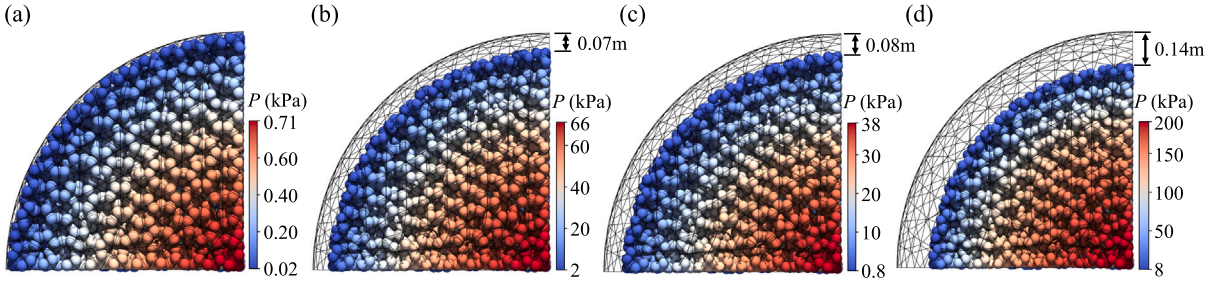

Fig. 15. Spatial distribution of pore pressure in Cryer's sphere for different λ_m values and hydraulic conductivity models. (a) $\lambda_m = 0.01$ with model SS1. (b) $\lambda_m = 0.1$ with model SS1. (c) $\lambda_m = 0.1$ with model SS2. (d) $\lambda_m = 0.25$ with model SS2.

4.7. Strip footing with mesh reconstruction

While the preceding examples were confined to elastic deformations, this section validates the proposed algorithm for consolidation problems involving large plastic deformations and severe mesh distortion. To this end, we investigate a strip footing problem, as depicted in Fig. 16a. The computational domain is discretized using approximately 5400 particles and elements, with the background mesh being locally refined in the vicinity of the loading area. The top surface to the right of the footing is permeable, while all other boundaries are impervious. The soil is modeled using the Tresca constitutive model with an undrained shear strength of $C_s = 1$ kPa. The elastic properties are defined by a Poisson's ratio of $\nu = 0.3$, and the hydraulic conductivity is $k = 1.0 \times 10^{-9}$ m/day. A constant downward velocity is prescribed to the rigid footing, which has a width of $B = 2$ m. This is achieved by applying a total vertical displacement of $U = -2$ m over a dimensionless time period of $T_v = 1$, which is completed in 200 steps. The dimensionless time factor, T_v, is defined as $T_v = \frac{Ekt}{2\gamma_w(1+\nu)(1-2\nu)B^2}$, where γ_w is the unit weight of pore water. This loading induces a resistance force, q, from the soil. The normalized resistance of the soil foundation is given by the $I_r = G/C_s$, where G is the shear modulus. Two cases with rigidity indices of $I_r = 16$ and $I_r = 33.4$ are analyzed.

To provide a theoretical benchmark, the analytical solutions proposed by Prandtl [74] ($(2+\pi)C_s$ for surface footing) and Meyerhof [75] ($(2 + 2\pi)C_s$ for deep embedment) are included. As shown in Fig. 16b, which plots normalized resistance (q/C_s) versus vertical displacement, HEPM effectively captures the transition from Prandtl's limit towards Meyerhof's limit as the footing penetrates deeper. The results show excellent agreement with SNS-PFEM and are also compared with UL-FEM. The UL-FEM analysis is presented to highlight its inherent limitations compared to remeshing strategy. Its predicted resistance-displacement curve diverges from the other methods, showing a lower reaction force before the simulation terminates prematurely. This is a direct consequence of severe mesh distortion, as elements near the rigid foundation undergo excessive tensile deformation. This distortion causes the Jacobian determinant to become non-positive, which not only artificially absorbs kinematic energy (leading to an underestimation of bearing capacity) but ultimately prevents the nonlinear solver from converging. In

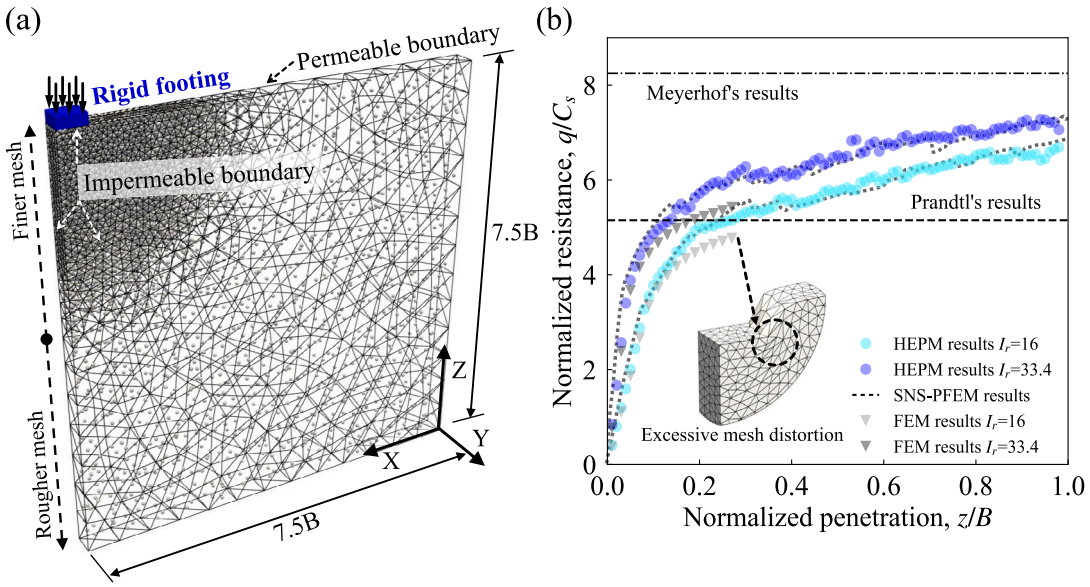

Fig. 16. Numerical simulation of strip footing penetration in saturated soil. (a) Schematic of the penetration model. (b) Comparison of normalized resistance obtained from HEPM, SNS-PFEM, and UL-FEM. The horizontal lines indicate the analytical bearing capacity limits: the dashed line for Prandtl (surface footing) and the dash-dotted line for Meyerhof (deep embedment).

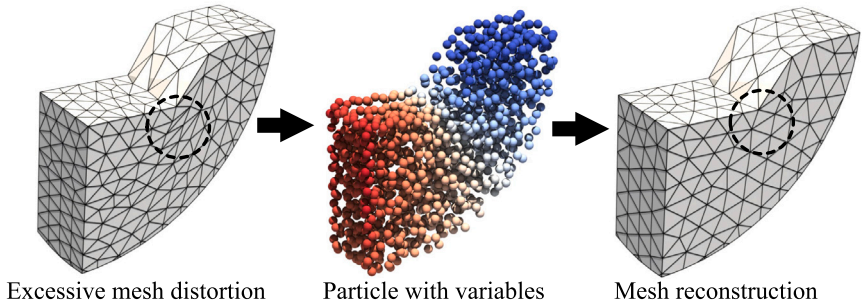

Fig. 17. Illustration of the remeshing strategy employed to mitigate excessive mesh distortion during consolidation. The distorted elements are discarded, leaving discrete particles to preserve history variables, after which a high-quality mesh is independently reconstructed for subsequent calculations.

contrast, the proposed HEPM fundamentally overcomes this limitation regarding convergence. Its exceptional robustness for handling extreme deformation stems from storing all physical state variables (such as stress and pore pressure) on independent Lagrangian particles (Fig. 17). This strategy decouples the solution data from the mesh, allowing the distorted mesh to be discarded and regenerated with high-quality elements as needed. As a result, the simulation can proceed through severe deformations without encountering Jacobian singularities, thereby ensuring both computational stability and robust convergence. Although this reconstruction process introduces minor numerical fluctuations, a phenomenon also observed in similar methods like PFEM, it is the key to successfully completing the large-deformation analysis.

Fig. 18 shows the equivalent plastic strain ($\bar{\varepsilon}_p$) and pore pressure (P) distributions for the footing penetration problem where I_r is 33.4. Specifically, the plastic strain contour in Fig. 18a delineates the characteristic shear failure mechanism that develops in the soil beneath the footing. A slight heave of the soil surface is observed adjacent to the footing, while a distinct shear band develops between the compressed zone beneath the footing and the adjacent heaved region. An elastic wedge is also seen to form directly under the footing, a phenomenon consistent with established geotechnical failure modes. Regarding the pore pressure distribution shown in Fig. 18b, the undrained loading condition beneath the footing leads to the generation of maximum pore water pressure in this area. This excess pressure then gradually dissipates radially outwards, exhibiting a clear diffusion pattern from the center to the outer regions. The comparison with the SNS-PFEM results highlights a key advantage of the proposed method. Notably, our framework yields a more uniform distribution of pore water pressure, effectively mitigating the pore pressure concentration at the edges of the rigid footing.

In short, while traditional mesh-based Lagrangian methods are prone to severe mesh distortion, the proposed FIC-stabilized HEPM fundamentally overcomes this limitation. Furthermore, when compared to other advanced particle methods, the present method yields a superior result by producing a more uniform pore pressure field, effectively suppressing spurious oscillations and concentrations.

4.8. Vertical cutting of a soil block

In this section, the robustness and applicability of the proposed HEPM are further demonstrated through the simulation of vertical cutting of a soil block, which is characterized by extreme material distortion and flow. Such problems, characterized by localized failure and large plastic strains, often pose significant challenges for traditional mesh-based methods due to severe mesh distortion. The proposed HEPM is particularly well-suited for this problem. The analysis in this section focuses on the formation of the failure surface and the corresponding pore pressure dissipation modes, and the simulation results are validated against numerical solutions from Navas et al. [76] and Yuan et al. [57].

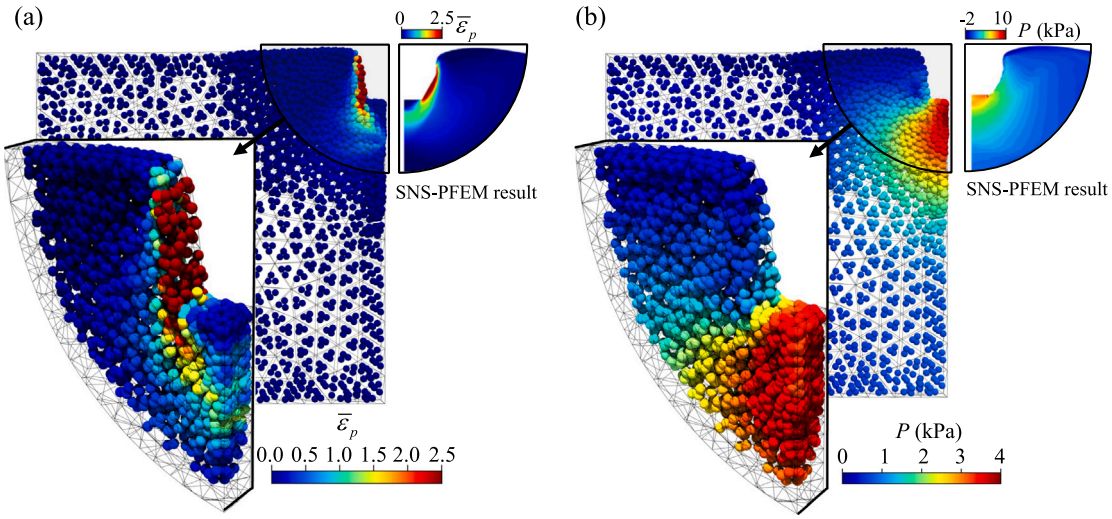

Fig. 18. Comparison of HEPM and reference SNS-PFEM solutions for the strip footing problem (I_r = 33.4). (a) Equivalent plastic strain contours showing the failure mechanism. (b) Pore pressure distribution showing the hydraulic response.

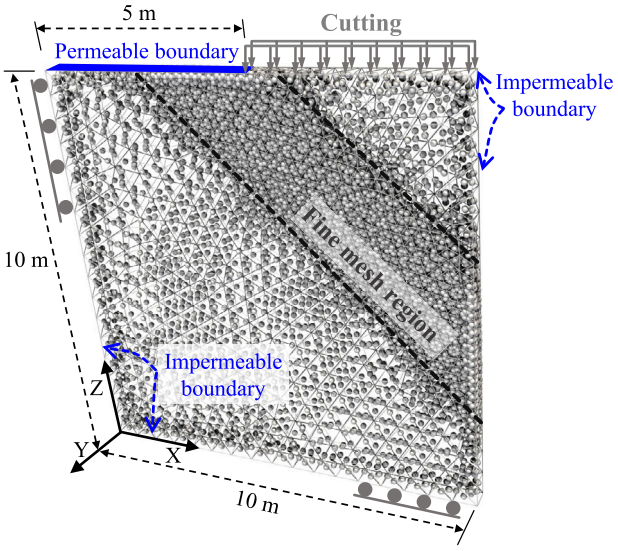

Fig. 19. Numerical setup and boundary conditions for the vertical cutting of a saturated soil block. The 10 m × 10 m domain employs a fine mesh along the expected shear path and specific permeable/impermeable boundaries to capture localized failure.

The model setup and boundary conditions are illustrated in Fig. 19. The soil domain is discretized using approximately 3400 particles, with a local region of finer mesh resolution applied along the anticipated failure plane to capture the development of plastic strain. The left and bottom boundaries are modeled as impermeable slip surfaces. The right boundary and the right half of the top boundary (the cutting area) is impermeable. The right boundary is an impermeable free surface, while the top free surface is impermeable in the cutting area on the right and permeable on the left to allow for drainage. A constant vertical cutting velocity of 0.2 m/s is applied to the top-right half of the soil block for a total duration of 75 s (completed in 150 time steps) to induce shear failure. The material behavior is described by a linear elastic model, with failure governed by the Drucker–Prager (DP) criterion. The specific parameters used for the simulation are listed in Table 3.

Table 3
Material properties for the shear consolidation analysis of vertical cutting.

Property	Value
Elastic modulus, E	9.175 MPa
Poisson ratio, ν	0.316
Cohesive strength, c	100 kPa
Dilatancy angle, ψ	0°
Friction angle, φ	20°
Hydraulic conductivity, k	10^{-4} m/s
Porosity, n	0.33

Fig. 20 illustrates the evolution of pore water pressure during a large-deformation vertical cutting analysis, comparing the results of the proposed method at two time step, t = 25 s and t = 45 s, with established reference solutions. As the footing penetrates the soil, a high pore water pressure develops directly beneath it. The progression from t = 25 s to t = 45 s clearly demonstrates the migration and expansion of this high-pressure region deeper into the soil domain. This dynamic process highlights the gradual dissipation and redistribution of pore water pressure over time. For validation purposes, a comparison is performed with the numerical results [57,76]. The pressure distributions predicted by our model exhibit agreement with both reference studies. Specifically, our method accurately captures the key features, including the location, shape, and magnitude of the compression-induced positive pressure region. This strong correlation underscores the capability and robustness of the proposed framework for analyzing complex, large-deformation coupled problems, particularly in condition where severe mesh distortion presents a primary challenge.

Fig. 21 illustrates the progressive formation of the shear band in terms of the equivalent plastic strain $\bar{\varepsilon}_p$ (PEEQ). In the initial stage (t = 25 s), a distinct shear band initiates from the edge of loading and propagates downward to the right into the soil domain at an angle of approximately 45°. Plastic strain is highly concentrated within this narrow zone, and its magnitude is most pronounced near the surface where deformation originates. As the penetration progresses to t = 45 s, the shear band becomes more clearly defined and extensive, both in depth and width. A significant intensification of plastic strain is observed, particularly in the upper portion of the band, indicating progressive failure localization along this surface. The comparison with reference

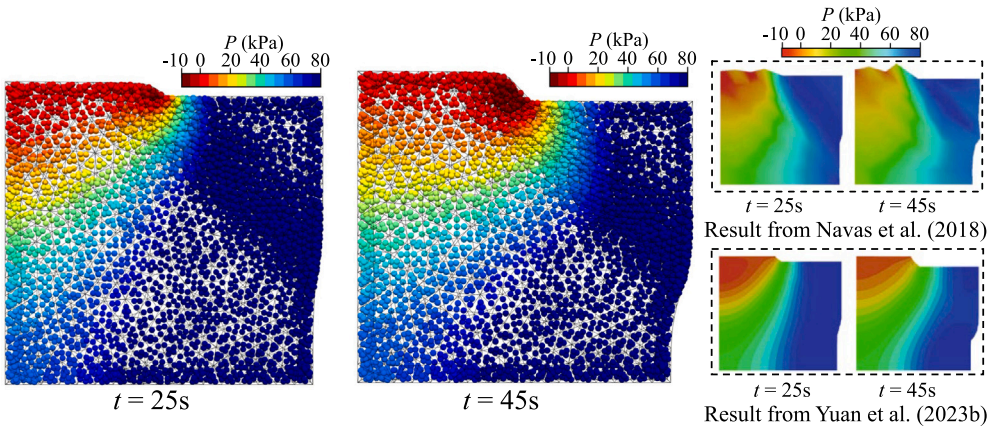

Fig. 20. Comparison of pore pressure distributions during the vertical cutting of saturated soil. The HEPM results at t = 25 s and t = 45 s are validated against reference solutions.

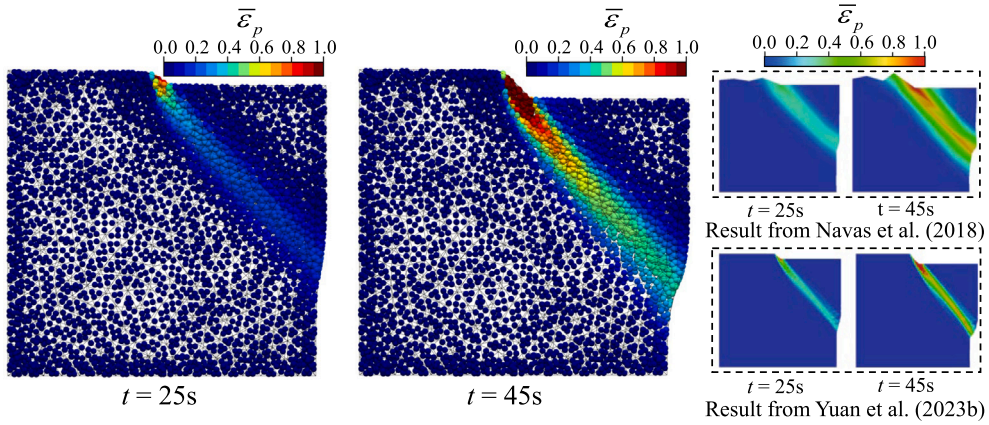

Fig. 21. Comparison of equivalent plastic strain during the vertical cutting of saturated soil. The HEPM results at t = 25 s and t = 45 s are validated against reference solutions.

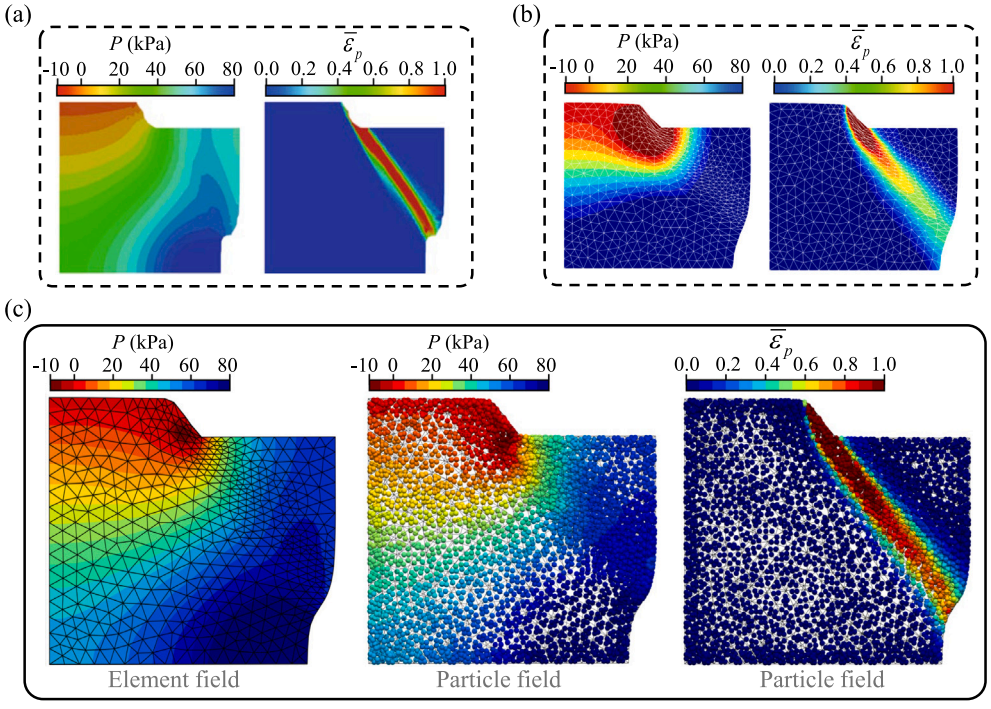

Fig. 22. Numerical results of the vertical cutting test at t = 75 s obtained by different methods. (a) SPFEM. (b) UL-FEM. (c) Proposed HEPM. The contours display pore pressure (left) and equivalent plastic strain (right).

results [57,76] reveals an excellent agreement in the overall failure mode, particularly concerning the inclination angle of the shear band and the pattern of strain localization. This consistency validates the capability of the proposed method to accurately capture characteristic soil failure mechanisms under consolidation.

Fig. 22 presents a comparison of these above results obtained from the proposed FIC-stabilized HEPM, SPFEM, and the UL-FEM at $t = 75$ s. As illustrated in Fig. 22b, the UL-FEM result exhibits the inherent limitations of conventional Lagrangian methods regarding computational accuracy induced by severe mesh distortion. This distortion along the shear band induces volumetric locking and degrades the quality of element shape functions. Specifically, the pore pressure exhibits abnormally slow dissipation, resulting in an unphysical retention of high pressure at the column base. Furthermore, the plastic strain fails to form a fully developed shear band, appearing instead as an incomplete zone confined to the upper part. By contrast, the results from the SPFEM (Fig. 22a) and the proposed HEPM (Fig. 22c) agree well with each other. Both methods successfully capture a fully developed shear band that propagates through the soil block. The pore pressure distribution is smooth, with pressures exceeding 80 kPa concentrated at the bottom right of the domain. This demonstrates the effectiveness of the proposed HEPM in preventing mesh distortion and maintaining computational accuracy under large deformations. A minor and localized negative pressure zone is observed at the top of the shear band in the HEPM result, which is considered a mechanical response of the tensile separation of the meshes.

In summary, the simulation demonstrates that the proposed method not only overcomes the failure of traditional FEM due to mesh distortion but also yields similar results that are comparable to those from other advanced methods like PFEM, highlighting its robustness and accuracy for large-deformation analysis.

5. Conclusions

In this study, the FIC-stabilized Hybrid Element Particle Method (HEPM) was successfully applied to solve the computational challenges in modeling the coupled hydro-mechanical response of saturated soils involving large deformations. Key advantages of the proposed approach stem from its dual discretization strategy using both mesh and particles. This strategy decouples material motion from the computational mesh to avoid mesh distortion in nonlinear large-deformation consolidation, while simultaneously ensuring the effective suppression of spurious pressure oscillations through the particle-based FIC stabilization. Moreover, numerical stability and spatial convergence are significantly enhanced using efficient low-order element pairs, even under conditions of extreme deformation and undrained loading.

Furthermore, by integrating finite strain theory with nonlinear hydraulic models, the proposed framework ensures accurate settlement analysis in soft soils while proving its adaptability to complex hydro-mechanical nonlinearities. The specific capability to reproduce smooth pore pressure distributions and continuous plastic shear bands demonstrates that dynamic mesh reconstruction serves not merely as a correction to facilitate convergence, but as a fundamental requirement for the accuracy of coupled large-deformation responses. Consequently, the proposed framework offers a rigorous and reliable computational tool for coupled hydro-mechanical analysis in geotechnical engineering, paving the way for more accurate predictions of failure mechanisms involving extensive plastic flow.

CRediT authorship contribution statement

Yuanyi Qiu: Writing – original draft, Visualization, Validation, Software, Methodology, Investigation, Formal analysis. **Zhen-Yu Yin:** Writing – review & editing, Supervision, Funding acquisition, Conceptualization. **Huangcheng Fang:** Writing – review & editing, Supervision, Software, Methodology.

Declaration of generative AI in scientific writing

During the preparation of this work the authors used "ChatGPT" in order to improve language. After using this tool, the authors reviewed and edited the content as needed and take full responsibility for the content of the published article.

Declaration of competing interest

The authors declare that they have no known competing financial interests or personal relationships that could have appeared to influence the work reported in this paper.

Acknowledgments

The authors gratefully acknowledge the financial support from the Research Grants Council (RGC) of the Hong Kong Special Administrative Region Government (HKSARG) of China under Grant Nos. 15229223, 15232224, and T22-607/24-N, and from the State Key Laboratory of Climate Resilience for Coastal Cities at the Hong Kong Polytechnic University.

Appendix A. Weak formulation and linearization in Updated Lagrangian framework

The constitutive integration associated for elastoplasticity is performed at the particle level, employing an implicit backward Euler return-mapping algorithm to compute the corrected stress and derive the consistent material tangent matrix. This procedure follows the standard computational plasticity framework used in classical FEM [77]. The detailed derivations for two of its key components—the incremental objective stress rate and the consistent material tangent matrix—are provided in Appendices A and B, respectively. For a comprehensive derivation of the specific constitutive model used here, interested readers are referred to our previous work [51]. In large-deformation consolidation analysis, the momentum conservation equations should be established on the deformed configuration. Its weak form can be obtained by divergence theorem:

$$\int_{\Omega^{t+\Delta t}} \frac{\partial \delta u_i}{\partial x_j^{t+\Delta t}} \sigma_{ij}^{t+\Delta t} d\Omega = \int_{\Gamma^{t+\Delta t}} \delta u_i t_i^{t+\Delta t} d\Gamma + \int_{\Omega^{t+\Delta t}} \delta u_i \rho^{t+\Delta t} b_i d\Omega, \tag{A.1}$$

where $\sigma_{ij}^{t+\Delta t}$ is the total Cauchy stress; $t_i^{t+\Delta t}$ represents the traction on the Neumann boundary $\Gamma^{t+\Delta t}$; $\delta \mathbf{u}$ is the test function; the body force vector b_i (i.e., gravity) is assumed to be constant. In order to convert the left-hand side of the above equation, which represents the virtual work of the coupling internal forces $\delta \Pi_{\text{int}}^{\text{K}}$, to a known configuration for integration, following transformation is used:

$$F_{ij} = \frac{\partial x_i^{t+\Delta t}}{\partial x_j^{t}} = \nabla^t x^{t+\Delta t}, \tag{A.2}$$

$$\mathrm{d}\Omega^{t+\Delta t} = J \mathrm{d}\Omega^t, \tag{A.3}$$

where $\mathbf{x}_i^t$ and $\mathbf{x}_i^{t+\Delta t}$ are the position vectors of a material point in the last known converged and current unknown configurations, respectively;

By mapping the $\delta \Pi_{\text{int}}^{\text{K}}$ from the current unknown configuration to the previous configuration, we obtain:

$$\delta \Pi_{\text{int}}^{\text{K}} = \int_{\Omega^t} \frac{\partial \delta u_i}{\partial x_j^t} F_{ij}^{-1} : J \sigma_{ij}^{t+\Delta t} d\Omega. \tag{A.4}$$

Further linearization of the internal virtual work expression with respect to the incremental displacement field yields:

$$\Delta(\delta \Pi_{\text{int}}^{\text{K}}) = \int_{\Omega^t} [\frac{\partial \delta u_i}{\partial x_j^t} (\Delta F_{ij}^{-1}) : J \sigma_{ij}^{t+\Delta t} + \frac{\partial \delta u_i}{\partial x_j^t} F_{ij}^{-1} : (\Delta J \sigma_{ij}^{t+\Delta t} + J \Delta \sigma_{ij})] d\Omega. \tag{A.5}$$

To formulate the consistent tangent stiffness matrix, the terms ΔJ and $\Delta(F_{ij}^{-1})$ in the equation above must be expressed in terms of the incremental displacement:

$$\Delta J = \Delta \det(F_{ij}) = J \frac{\partial \Delta u_i}{\partial x_i^{t+\Delta t}}, \tag{A.6}$$

$$\Delta({F_{ij}}^{-1}) = -{F_{ik}}^{-1} \frac{\partial \Delta u_k}{\partial x_j^{t+\Delta t}}. \tag{A.7}$$

By substituting Eqs. (A.6) and (A.7) into the linearized virtual work equation, we can further obtain

$$\Delta(\delta \Pi_{\text{int}}^{\text{K}}) = \int_{\Omega^{t+\Delta t}} \frac{\partial \delta u_i}{\partial x_j^{t+\Delta t}} \left[\Delta \sigma_{ij}^{t+\Delta t} - \sigma_{il}^{t+\Delta t} \frac{\partial \Delta u_j}{\partial x_l^{t+\Delta t}} + \sigma_{ij}^{t+\Delta t} \frac{\partial \Delta u_k}{\partial x_k^{t+\Delta t}} \right] d\Omega, \tag{A.8}$$

where $\Delta \sigma_{ij} = \dot{\sigma}_{ij} \Delta t$ and $\Delta u_i = \dot{u}_i \Delta t$.

By substituting principle of effective stress and Eq. (C.4) into Eq. (A.8), the governing equations are rewritten as:

$$\Delta(\delta \Pi_{\text{int}}^{\text{K}}) = \int_{\Omega^{t+\Delta t}} \frac{\partial \delta u_i}{\partial x_j^{t+\Delta t}} \left[C_{ijkl} \frac{\partial \Delta u_k}{\partial x_l^{t+\Delta t}} - \alpha \delta_{ij} \Delta p - \sigma_{il} \frac{\partial \Delta u_j}{\partial x_l^{t+\Delta t}} + \sigma_{ij} \frac{\partial \Delta u_k}{\partial x_k^{t+\Delta t}} \right] d\Omega. \tag{A.9}$$

To solve the nonlinear system, a Newton–Raphson iterative scheme is adopted. Assuming deformation-independent external forces, the linearized system for the ith iteration is formulated as follows, where the incremental internal virtual work has been expressed in a compact tensor form for simplicity:

$$\int_{\Omega_{t+\Delta t}^{[i]}} \nabla^{t+\Delta t}(\delta \mathbf{u}^{[i]}) : \left\{ \mathbf{C} : \nabla^{t+\Delta t}(\Delta \mathbf{u}) - \alpha \Delta p \mathbf{I} + \boldsymbol{\sigma}^{t+\Delta t} \left[\nabla^{t+\Delta t} \cdot \Delta \mathbf{u} - (\nabla^{t+\Delta t} \Delta \mathbf{u})^T \right] \right\}^{[i]} d\Omega = (\mathbf{r}^{t+\Delta t})^{[i]}, \tag{A.10}$$

where $(\mathbf{r}^{t+\Delta t})^{[i]}$ is the residual vector at the ith iteration. It is computed as:

$$(\mathbf{r}^{t+\Delta t})^{[i]} = \int_{\Omega_{t+\Delta t}^{[i]}} \delta \mathbf{u}^{[i]} \cdot \rho^{[i]} \mathbf{b} d\Omega + \int_{\Gamma_{t+\Delta t}^{[i]}} \delta \mathbf{u}^{[i]} \cdot \mathbf{t}^{t+\Delta t} d\Gamma - \int_{\Omega_{t+\Delta t}^{[i]}} \nabla^{t+\Delta t} \delta \mathbf{u}^{[i]} : (\boldsymbol{\sigma}^{t+\Delta t})^{[i]} d\Omega. \tag{A.11}$$

The weak form of the mass balance equation in large-deformation analysis can also be obtained on the current configuration. Starting from the governing equation Eq. (2), the weak form for the current configuration is obtained by applying the divergence theorem:

$$\int_{\Omega_{t+\Delta t}} \delta p \left(m \frac{\partial p}{\partial t} \right) d\Omega + \int_{\Omega_{t+\Delta t}} \delta p \alpha \frac{1}{J} \frac{\partial (J)}{\partial t} d\Omega + \int_{\Omega_{t+\Delta t}} \nabla \delta p \cdot \frac{\mathbf{k}}{\mu_w} \nabla p d\Omega = \int_{\Omega_{t+\Delta t}} \delta p \cdot Q d\Omega - \int_{\Gamma_{w t+\Delta t}} \delta p \frac{q_w}{\rho_w} d\Gamma, \tag{A.12}$$

where $m = \left(\frac{\alpha - n}{K_s} + \frac{n}{K_w} \right)$ is the total compressibility. For a more convenient linearization, the equation is first discretized in time using a fully implicit backward Euler scheme:

$$\int_{\Omega^{t+\Delta t}} \delta p \, m(p^{t+\Delta t} - p^t) d\Omega + \int_{\Omega^{t+\Delta t}} \delta p \, \alpha \frac{(J-1)}{J} d\Omega + \Delta t \int_{\Omega^{t+\Delta t}} \nabla^{t+\Delta t} \delta p \cdot \frac{\mathbf{k}}{\mu_w} \nabla^{t+\Delta t} p^{t+\Delta t} d\Omega = \Delta t (\mathbf{F}_p^{t+\Delta t}), \tag{A.13}$$

where $\mathbf{F}_p^{t+\Delta t}$ represents the right-hand side in Eq. (A.12). Then, pulling the equation back to the configuration at time t yields:

$$\underbrace{\int_{\Omega^t} \delta p \, m(p^{t+\Delta t} - p^t) J d\Omega}_{\text{Compressibility term}} + \underbrace{\int_{\Omega^t} \delta p \, \alpha (J-1) d\Omega}_{\text{Coupling term}} + \underbrace{\Delta t \int_{\Omega^t} [(\nabla^t \delta p) \cdot \boldsymbol{F}^{-1}] \cdot (\nabla^t p^{t+\Delta t} \cdot \boldsymbol{F}^{-1}) \frac{\mathbf{k}}{\mu_w} J d\Omega}_{\text{Permeability term}} = \Delta t (\mathbf{F}_p^{t+\Delta t}). \tag{A.14}$$

The left-hand side of the governing equation is subsequently linearized by taking the total differential. The linearization of the compressibility term yields:

$$\Delta(\delta \Pi_{\text{int}}^{\text{M}}) = \int_{\Omega^t} \delta p \, m \left[(p^{t+\Delta t} - p^t) \cdot \Delta J + J \cdot \Delta p \right] d\Omega. \tag{A.15}$$

The linearization of the coupling term is given by:

$$\Delta(\delta \Pi_{\text{int}}^{\text{C}}) = \int_{\Omega^t} \delta p \, \alpha \cdot \Delta J d\Omega. \tag{A.16}$$

Finally, the linearization of the permeability term results in:

$$\begin{aligned} \Delta(\delta \Pi_{\text{int}}^{\text{H}}) = \Delta t \int_{\Omega^t} \frac{\mathbf{k}}{\mu_w} \Big\{ & \left[(\nabla^t \delta p) \cdot \Delta \boldsymbol{F}^{-1} \right] \cdot (\nabla^t p^{t+\Delta t} \cdot \boldsymbol{F}^{-1}) J \\ & + \left[(\nabla^t \delta p) \cdot \boldsymbol{F}^{-1} \right] \cdot (\nabla^t \Delta p \cdot \boldsymbol{F}^{-1} + \nabla^t p^{t+\Delta t} \cdot \Delta \boldsymbol{F}^{-1}) J \\ & + \left[(\nabla^t \delta p) \cdot \boldsymbol{F}^{-1} \right] \cdot (\nabla^t p^{t+\Delta t} \cdot \boldsymbol{F}^{-1}) \Delta J \Big\} d\Omega. \end{aligned} \tag{A.17}$$

By substituting Eqs. (A.6) and (A.7), then pushing forward to the current configuration at $t + \Delta t$ gives:

$$\begin{aligned} \Delta(\delta \Pi_{\text{int}}^{\text{M}} + \delta \Pi_{\text{int}}^{\text{C}} + \delta \Pi_{\text{int}}^{\text{H}}) = & \int_{\Omega^{t+\Delta t}} \delta p \, m \left[(p^{t+\Delta t} - p^t)(\nabla^{t+\Delta t} \cdot \Delta \mathbf{u}) + \Delta p \right] d\Omega \\ & + \int_{\Omega^{t+\Delta t}} \delta p \, \alpha (\nabla^{t+\Delta t} \cdot \Delta \mathbf{u}) d\Omega \\ & + \Delta t \int_{\Omega^{t+\Delta t}} \frac{\mathbf{k}}{\mu_w} \Big\{ \\ & \quad - [(\nabla^{t+\Delta t} \delta p) \cdot (\nabla^{t+\Delta t} \Delta \mathbf{u})] \cdot (\nabla^{t+\Delta t} p_w^{t+\Delta t}) \\ & \quad + (\nabla^{t+\Delta t} \delta p) \cdot (\nabla^{t+\Delta t} \Delta p - (\nabla^{t+\Delta t} p^{t+\Delta t}) \cdot (\nabla^{t+\Delta t} \Delta \mathbf{u})) \\ & \quad + [(\nabla^{t+\Delta t} \delta p)] \cdot (\nabla^{t+\Delta t} p^{t+\Delta t})(\nabla^{t+\Delta t} \cdot \Delta \mathbf{u}) \Big\} d\Omega. \end{aligned} \tag{A.18}$$

Combining like terms simplifies the expression. The resulting Newton iteration for the updated Lagrangian method, assuming deformation-independent boundary terms, is:

$$\begin{aligned} & \int_{\Omega_{t+\Delta t}^{[i]}} \delta p^{[i]} \alpha \nabla^{t+\Delta t} \cdot (\Delta \mathbf{u}^{[i]}) d\Omega + \int_{\Omega_{t+\Delta t}^{[i]}} \delta p^{[i]} m \Delta p^{[i]} d\Omega \\ & \quad + \Delta t \int_{\Omega_{t+\Delta t}^{[i]}} (\nabla^{t+\Delta t} \delta p^{[i]}) \cdot \frac{\mathbf{k}}{\mu_w} \cdot (\nabla^{t+\Delta t} \Delta p^{[i]}) d\Omega \\ & + \int_{\Omega_{t+\Delta t}^{[i]}} \delta p^{[i]} m [(p^{t+\Delta t})^{[i]} - p^t] (\nabla^{t+\Delta t} \cdot \Delta \mathbf{u})^{[i]} d\Omega \\ & + \Delta t \int_{\Omega_{t+\Delta t}^{[i]}} (\nabla^{t+\Delta t} \delta p^{[i]}) \cdot \frac{\mathbf{k}}{\mu_w} \cdot \nabla^{t+\Delta t} p^{[i]} (\nabla^{t+\Delta t} \cdot \Delta \mathbf{u})^{[i]} d\Omega \\ & - \Delta t \int_{\Omega_{t+\Delta t}^{[i]}} (\nabla^{t+\Delta t} \delta p^{[i]}) \cdot \frac{\mathbf{k}}{\mu_w} \cdot \left[\nabla^{t+\Delta t} \Delta \mathbf{u}^{[i]} + (\nabla^{t+\Delta t} \Delta \mathbf{u}^{[i]})^T \right] \cdot \nabla^{t+\Delta t} p^{[i]} d\Omega = (r_p^{t+\Delta t})^{[i]}, \end{aligned} \tag{A.19}$$

with the residual force is given by:

$$\begin{aligned} (r_p^{t+\Delta t})^{[i]} = & \Delta t \left(\int_{\Omega^{t+\Delta t}} \delta p^{[i]} Q^{t+\Delta t} d\Omega - \int_{\Gamma_w^{t+\Delta t}} \delta p^{[i]} \frac{q_w^{t+\Delta t}}{\rho_w} d\Gamma \right) \\ & - \int_{\Omega^{t+\Delta t}} \delta p^{[i]} \, m (p^{t+\Delta t} - p^t)^{[i]} d\Omega - \int_{\Omega^{t+\Delta t}} \delta p^{[i]} \, \alpha \left(\frac{J-1}{J} \right)^{[i]} d\Omega \\ & - \Delta t \int_{\Omega^{t+\Delta t}} \nabla^{t+\Delta t} \delta p^{[i]} \cdot \frac{\mathbf{k}}{\mu_w} \nabla^{t+\Delta t} (p^{t+\Delta t})^{[i]} d\Omega, \end{aligned} \tag{A.20}$$

where the superscript/subscript $[i]$ denotes the iteration count and the source and boundary flux terms are assumed to be deformation-independent.

Appendix B. Incrementally objective integration algorithm

For path-dependent materials, the mechanical response cannot be fully characterized solely by the initial and final strain states. This necessitates rate-form constitutive equations, which provide a rigorous

theoretical foundation for numerical integration algorithms. A key concept is the objective stress rate, which is necessary because the material time derivative of the Cauchy stress is not objective. Numerous objective stress rates have been proposed, with the Jaumann stress rate being a widely used example:

$$\dot{\sigma}'_{ij} = \dot{\sigma}'^{J}_{ij} + \left(\sigma'_{ik}\cdot\dot{\omega}_{kj} + \sigma'_{jk}\cdot\dot{\omega}_{ki}\right), \text{with} \quad \dot{\sigma}'^{J}_{ij} = D_{ijkl} : \varepsilon_{kl} \tag{B.1}$$

Here, D_{ijkl} is the constitutive tensor; σ'_{ij} is the effective Cauchy stress and $\dot{\sigma}'_{ij}$ is its objective rate, decomposed into constitutive response $\dot{\sigma}'^{J}_{ij}$ and a rotation term, quantified by the rate of spin tensor $\dot{\omega}_{ij}$. A known limitation of the Jaumann rate is that its objectivity cannot be guaranteed when used in implicit analyses with significant time increments [78].

Instead, the Hughes–Winget incrementally objective integration scheme [79] is adopted to integrate the rate constitutive equations:

$${}^{t+\Delta t}\sigma'_{ij} = \hat{\sigma}'_{ij} + \Delta\sigma'_{ij}, \text{ with } \hat{\sigma}'_{ij} = R_{ik}\,{}^{t}\sigma'_{kl}R_{jl} \tag{B.2}$$

where $\Delta\sigma'_{ij}$ is the incremental form of stress rate; R_{ij} is the rotation matrix can be constructed explicitly from $\Delta\omega_{ij}$ using the generalized midpoint rule, which ensures incremental objectivity:

$$R_{ij} = \delta_{ij} + \left(\delta_{ik} - \frac{1}{2}\Delta\omega_{ik}\right)^{-1}\Delta\omega_{kj} \tag{B.3}$$

In the same way, the strain and the spin increments are evaluated at the midpoint of the increment:

$$\Delta\varepsilon_{ij} = \frac{1}{2}\left(\frac{\partial\Delta u_i}{\partial^{t+\Delta t/2}x_j} + \frac{\partial\Delta u_j}{\partial^{t+\Delta t/2}x_i}\right), \quad \Delta\omega_{ij} = \frac{1}{2}\left(\frac{\partial\Delta u_i}{\partial^{t+\Delta t/2}x_j} - \frac{\partial\Delta u_j}{\partial^{t+\Delta t/2}x_i}\right) \tag{B.4}$$

where Δu_i is the displacement incremental from time t to $t+\Delta t$. Subsequently, the stress within the rotated coordinate system is linearized and the its rate is given by taking the time derivatives of $\hat{\sigma}'_{ij}$:

$$\dot{\hat{\sigma}}'_{ij} = \dot{R}_{ik}\,{}^{t}\sigma'_{kl}R_{jl} + R_{ik}\,{}^{t}\sigma'_{kl}\dot{R}_{jl} = \sum_{k,l}\left(\delta_{ik}R_{jp}\,{}^{t}\sigma'_{lp} + \delta_{jk}R_{ip}\,{}^{t}\sigma'_{pl}\right)\dot{R}_{kl} = \mathbf{S} : \dot{\mathbf{R}} \tag{B.5}$$

where the time derivatives of $\Delta\varepsilon_{ij}$, $\Delta\omega_{ij}$, and R_{ij} yields:

$$\dot{R}_{ij} = \left[(2\delta_{ik} - \hat{\omega}_{ik})^{-1}(\delta_{lj} + R_{lj})\right]\dot{\hat{\omega}}_{kl} = \sum_{k,l}H_{ijkl}\dot{\hat{\omega}}_{kl} = \mathbf{H} : \dot{\hat{\boldsymbol{\omega}}} \tag{B.6}$$

$$\begin{aligned}\dot{\varepsilon}_{ij} &= \frac{1}{2}\left(\frac{\partial^t x_i}{\partial^{t+\Delta t/2}x_k}\frac{\partial^{t+\Delta t}x_l}{\partial^{t+\Delta t/2}x_j} + \frac{\partial^t x_j}{\partial^{t+\Delta t/2}x_k}\frac{\partial^{t+\Delta t}x_l}{\partial^{t+\Delta t/2}x_i}\right)\frac{\partial\dot{u}_k}{\partial^{t+\Delta t}x_l}\\ &= \sum_{k,l}M_{ijkl}\frac{\partial\dot{u}_k}{\partial^{t+\Delta t}x_l} = \mathbf{M} : {}^{t+\Delta t}\nabla\dot{\mathbf{u}}\end{aligned} \tag{B.7}$$

$$\begin{aligned}\omega_{ij} &= \frac{1}{2}\left(\frac{\partial^t x_i}{\partial^{t+\Delta t/2}x_k}\frac{\partial^{t+\Delta t}x_l}{\partial^{t+\Delta t/2}x_j} - \frac{\partial^t x_j}{\partial^{t+\Delta t/2}x_k}\frac{\partial^{t+\Delta t}x_l}{\partial^{t+\Delta t/2}x_i}\right)\frac{\partial\dot{u}_k}{\partial^{t+\Delta t}x_l}\\ &= \sum_{k,l}P_{ijkl}\frac{\partial\dot{u}_k}{\partial^{t+\Delta t}x_l} = \mathbf{P} : {}^{t+\Delta t}\nabla\dot{\mathbf{u}}\end{aligned} \tag{B.8}$$

where the operator $\nabla^{t+\Delta t}$ denotes the spatial gradient evaluated with respect to the coordinates at the midpoint configuration $t+\Delta t$. Finally, by substituting the Eqs. (B.6)–(B.8) into the Eq. (B.5), we can establish the relationship between objective effective stress rate and displacement gradient:

$$\dot{\hat{\sigma}}'_{ij} = \dot{\hat{\boldsymbol{\sigma}}} = \mathbf{Y} : \nabla^{t+\Delta t}\dot{\mathbf{u}}, \text{ with } \mathbf{Y} = \mathbf{S} : \mathbf{H} : \mathbf{P} \tag{B.9}$$

Appendix C. Consistent tangent for hypoelasticity material

The constitutive behavior of hypoelasticity material is typically formulated in an incremental manner, linking the stress increment to the strain increment over a small step. The total strain increment $\Delta\varepsilon_{ij}$ can be decomposed into an elastic component $\Delta\varepsilon^{e}_{ij}$, and a plastic component $\Delta\varepsilon^{p}_{ij}$:

$$\Delta\varepsilon_{ij} = \Delta\varepsilon^{e}_{ij} + \Delta\varepsilon^{p}_{ij} \tag{C.1}$$

$$\Delta\varepsilon^{p}_{ij} = \aleph_{ij}\Delta\lambda, \text{ with } \aleph_{ij} = \frac{\partial g({}^{t+\Delta t}\sigma'_{ij}, c_y)}{\partial\sigma'_{ij}} \tag{C.2}$$

where $\Delta\lambda$ is the plastic multiplier and its direction $\aleph_{kl}$ is governed by the gradient of a plastic potential function $g(*)$; c_y is the strength parameter set. By substituting Eqs. (C.1) and (C.2) into Eq. (B.2), we arrive at the stress update equation with yield criterion $f(*)$ used in return-mapping algorithms by the backward Euler method:

$${\sigma_{ij}}'^{t+\Delta t} = \hat{\sigma}'_{ij} + D^{e}_{ijkl}(\Delta\varepsilon_{kl} - \aleph_{kl}\Delta\lambda), \text{ with } f(\sigma'^{t+\Delta t}_{ij}, c_y) = 0 \tag{C.3}$$

where D^{e}_{ijkl} is the fourth-order tensor of elastic module.

Finally, the consistent tangent modulus for large-deformation plasticity, $\mathbf{C}$, is obtained by taking the time derivative of the stress update scheme, a procedure that incorporates the strain increment defined in Eq. (B.7). This fourth-order tensor then establishes the linear relationship between the objective stress rate and the velocity gradient:

$$\dot{\sigma}'_{ij} = C_{ijkl}\frac{\partial\dot{u}_k}{\partial^{t+\Delta t}x_l} = \mathbf{C} : {}^{t+\Delta t}\nabla\dot{\mathbf{u}} \tag{C.4}$$

where $\mathbf{C}$ is composed of two distinct parts: a material stiffness term Eq. (B.7) and a rotational stiffness term arising from the objective stress rate formulation Eq. (B.9), expressed as:

$$\mathbf{C} = \mathbf{D}_{\text{mat}}\mathbf{M} + \mathbf{D}_{\text{rot}}\mathbf{Y} \tag{C.5}$$

where $\mathbf{D}_{\text{mat}}$ is the material tangent stiffness tensor, $\mathbf{D}_{\text{rot}}$ represents the contributions from the objective stress rate. A detailed derivation of this consistent tangent modulus is omitted for brevity; interested readers are referred to Fish and Shek [79] and Fang and Yin [51].

Data availability

Data will be made available on request.

References

[1] Xu Q, Zhao B, Dai K, Dong X, Li W, Zhu X, Yang Y, Xiao X, Wang X, Huang J, et al. Remote sensing for landslide investigations: A progress report from China. Eng Geol 2023;321:107156.

[2] Qiu H, Su L, Tang B, Yang D, Ullah M, Zhu Y, Kamp U. The effect of location and geometric properties of landslides caused by rainstorms and earthquakes. Earth Surf Process Landf 2024;49(7):2067–79.

[3] Kimoto S, Oka F, Fushita T. A chemo–thermo–mechanically coupled analysis of ground deformation induced by gas hydrate dissociation. Int J Mech Sci 2010;52(2):365–76.

[4] Di H, Zhou S, Xiao J, Gong Q, Luo Z. Investigation of the long-term settlement of a cut-and-cover metro tunnel in a soft deposit. Eng Geol 2016;204:33–40.

[5] Liu L, Li Z, Cai G, Geng X, Dai B. Performance and prediction of long-term settlement in road embankments constructed with recycled construction and demolition waste. Acta Geotech 2022;17(9):4069–93.

[6] Far H. Advanced computation methods for soil-structure interaction analysis of structures resting on soft soils. Int J Geotech Eng 2019;13(4):352–9.

[7] Qi S, Knappett JA. Effect of soil permeability on soil–structure and structure–soil–structure interaction of low-rise structures. Géotechnique 2022;72(9):784–99.

[8] Li S, Li C, Yao D, Liu C. Interdisciplinary asperity theory to analyze nonlinear motion of loess landslides with weak sliding interface. Landslides 2020;17(12):2957–65.

[9] Wen H, Xiao J, Xiang X, Wang X, Zhang W. Singular spectrum analysis-based hybrid PSO-gsa-SVR model for predicting displacement of step-like landslides: A case of jiuxianping landslide. Acta Geotech 2024;19(4):1835–52.

[10] Reddy JN. An introduction to nonlinear finite element analysis: with applications to heat transfer, fluid mechanics, and solid mechanics. Oxford University Press; 2015.

[11] Hong S, Kim H, Lee M-G. Anisotropic plasticity identification: Integrated FE and sensitivity-based virtual fields method. Int J Mech Sci 2025;110815.

[12] Kutlu A, Omurtag MH. Large deflection bending analysis of elliptic plates on orthotropic elastic foundation with mixed finite element method. Int J Mech Sci 2012;65(1):64–74.
[13] Rawat S, Gupta A. Analysis of a nailed soil slope using limit equilibrium and finite element methods. Int J Geosynth Ground Eng 2016;2(4):34.
[14] Li J, Zhou Y, Zhang L, Tian Y, Cassidy M, Zhang L. Random finite element method for spudcan foundations in spatially variable soils. Eng Geol 2016;205:146–55.
[15] Lee S, Kim K. Densification behavior of aluminum alloy powder under cold compaction. Int J Mech Sci 2002;44(7):1295–308.
[16] Zhang H, Fu Z, Wu J. Coupling multiscale finite element method for consolidation analysis of heterogeneous saturated porous media. Adv Water Resour 2009;32(2):268–79.
[17] Ni A, Shi Z, Meng Q. Broadband surface wave attenuation in porous soil by elastic metasurfaces. Int J Mech Sci 2024;264:108838.
[18] Wu X-H, Zhang Q, Feng W-Q, Yin Z-Y, Fang H. Enhanced thm coupling for anisotropic geomaterials and smoothed-fem simulation. Int J Mech Sci 2025;290:110087.
[19] Khoei A, Nikbakht M. An enriched finite element algorithm for numerical computation of contact friction problems. Int J Mech Sci 2007;49(2):183–99.
[20] Cervera M, Chiumenti M, Benedetti L, Codina R. Mixed stabilized finite element methods in nonlinear solid mechanics. Part III: Compressible and incompressible plasticity. Comput Methods Appl Mech Engrg 2015;285:752–75.
[21] Zhao C, Chen C, Zeng C, Bai W, Dai J. Novel periodic pile barrier with low-frequency wide bandgap for Rayleigh waves. Int J Mech Sci 2023;243:108006.
[22] Zeng W, Liu G. Smoothed finite element methods (S-FEM): an overview and recent developments. Arch Comput Methods Eng 2018;25(2):397–435.
[23] Gadala MS, Wang J. ALE formulation and its application in solid mechanics. Comput Methods Appl Mech Engrg 1998;167(1–2):33–55.
[24] Liu S, Tang X, Li J. Extension of ALE method in large deformation analysis of saturated soil under earthquake loading. Comput Geotech 2021;133:104056.
[25] Pastor M, Tayyebi SM, Stickle MM, Molinos M, Yague A, Manzanal D, Navas P. An arbitrary Lagrangian Eulerian (ALE) finite difference (FD)-SPH depth integrated model for pore pressure evolution on landslides over erodible terrains. Int J Numer Anal Methods Geomech 2022;46(6):1127–53.
[26] Foucard L, Aryal A, Duddu R, Vernerey F. A coupled Eulerian–Lagrangian extended finite element formulation for simulating large deformations in hyperelastic media with moving free boundaries. Comput Methods Appl Mech Engrg 2015;283:280–302.
[27] Fang H, Yin Z-Y, Zhang D, Cao L. A hydro-mechanical coupled contact method for two-phase geotechnical large deformation problems within the SNS-PFEM framework. Comput Methods Appl Mech Engrg 2024;420:116743.
[28] Zhao S, Niu R, Lu X, Wu C, Li S. A novel node-based smoothed polygonal finite element method with reconstructed strain fields for solving heat conduction problems. Int J Heat Mass Transfer 2025;248:127195.
[29] Cremonesi M, Franci A, Idelsohn S, Oñate E, et al. A state of the art review of the particle finite element method (PFEM). Arch Comput Methods Eng 2020;27(5):1709–35.
[30] Yu L-J, Jin Y-F, Yin Z-Y, Chen J-F. A novel stabilized nodal integration formulation using particle finite element method for incompressible flow analysis. Internat J Numer Methods Fluids 2024;96(6):853–83.
[31] Bui HH, Fukagawa R, Sako K, Ohno S. Lagrangian meshfree particles method (SPH) for large deformation and failure flows of geomaterial using elastic–plastic soil constitutive model. Int J Numer Anal Methods Geomech 2008;32(12):1537–70.
[32] Bui HH, Fukagawa R. An improved SPH method for saturated soils and its application to investigate the mechanisms of embankment failure: Case of hydrostatic pore-water pressure. Int J Numer Anal Methods Geomech 2013;37(1):31–50.
[33] Ma G, Bui HH, Lian Y, Tran KM, Nguyen GD. A five-phase approach, SPH framework and applications for predictions of seepage-induced internal erosion and failure in unsaturated/saturated porous media. Comput Methods Appl Mech Engrg 2022;401:115614.
[34] Feng R, Fourtakas G, Rogers BD, Lombardi D. A general smoothed particle hydrodynamics (SPH) formulation for coupled liquid flow and solid deformation in porous media. Comput Methods Appl Mech Engrg 2024;419:116581.
[35] Lian Y, Bui HH, Nguyen GD, Zhao S, Haque A. A computationally efficient SPH framework for unsaturated soils and its application to predicting the entire rainfall-induced slope failure process. Géotechnique 2024;74(8):787–805.
[36] Zhang S, Lourenço SD, Hu X. Multiphase SPH for surface tension: Resolving zero-surface-energy modes and achieving high Reynolds number simulations. Comput Methods Appl Mech Engrg 2025;444:118147.
[37] Michel J, Colagrossi A, Antuono M, Marrone S. A regularized high-order diffusive smoothed particle hydrodynamics scheme without tensile instability. Phys Fluids 2023;35(10).
[38] Khayyer A, Shimizu Y, Lee CH, Gil A, Gotoh H, Bonet J. An improved updated Lagrangian SPH method for structural modelling. Comput Part Mech 2024;11(3):1055–86.
[39] Hoang TN, Bui HH, Nguyen TT, Nguyen TV, Nguyen GD. Development of free-field and compliant base SPH boundary conditions for large deformation seismic response analysis of geomechanics problems. Comput Methods Appl Mech Engrg 2024;432:117370.
[40] Modaressi H, Aubert P. Element-free Galerkin method for deforming multiphase porous media. Internat J Numer Methods Engrg 1998;42(2):313–40.
[41] Samimi S, Pak A. A fully coupled element-free Galerkin model for hydro-mechanical analysis of advancement of fluid-driven fractures in porous media. Int J Numer Anal Methods Geomech 2016;40(16):2178–206.
[42] Kularathna S, Liang W, Zhao T, Chandra B, Zhao J, Soga K. A semi-implicit material point method based on fractional-step method for saturated soil. Int J Numer Anal Methods Geomech 2021;45(10):1405–36.
[43] Liang W, Zhao J, Wu H, Soga K. Multiscale, multiphysics modeling of saturated granular materials in large deformation. Comput Methods Appl Mech Engrg 2023;405:115871.
[44] Zheng X, Wang S, Yang F, Yang J. Material point method simulation of hydro-mechanical behaviour in two-phase porous geomaterials: A state-of-the-art review. J Rock Mech Geotech Eng 2024;16(6):2341–50.
[45] Yu J, Zhao J, Zhao S, Liang W. Thermo-hydro-mechanical coupled material point method for modeling freezing and thawing of porous media. Int J Numer Anal Methods Geomech 2024;48(13):3308–49.
[46] Bandara S, Soga K. Coupling of soil deformation and pore fluid flow using material point method. Comput Geotech 2015;63:199–214.
[47] Yu J, Zhao J, Liang W, Zhao S. A semi-implicit material point method for coupled thermo-hydro-mechanical simulation of saturated porous media in large deformation. Comput Methods Appl Mech Engrg 2024;418:116462.
[48] de Vaucorbeil A, Nguyen VP. Modelling contacts with a total Lagrangian material point method. Comput Methods Appl Mech Engrg 2021;373:113503.
[49] Nguyen VP, De Vaucorbeil A, Bordas S. The material point method. Cham: Springer Int Publ 2023.
[50] Pretti G, Bird RE, Coombs WM, Augarde CE, Giani S. The stress-continuous material point method: A technique to alleviate cell-crossing instability while retaining linear shape functions. Comput Methods Appl Mech Engrg 2025;446:118168.
[51] Fang H, Yin Z-Y. A novel hybrid particle element method (HPEM) for large deformation analysis in solid mechanics. Comput Methods Appl Mech Engrg 2025;433:117530.
[52] Huangcheng F, Zhen-Yu Y. Lagrangian hybrid element particle method (LHEPM) for incompressible fluid dynamics. J Comput Phys 2025;114281.
[53] Lacroix M, Fernández E, Février S, Papeleux L, Boman R, Ponthot J-P. An efficient level set-based mesh adaptation for the particle finite element method. Comput Methods Appl Mech Engrg 2026;450:118644.
[54] Brezzi F, Bathe K-J. A discourse on the stability conditions for mixed finite element formulations. Comput Methods Appl Mech Engrg 1990;82(1–3):27–57.
[55] Sun W, Ostien JT, Salinger AG. A stabilized assumed deformation gradient finite element formulation for strongly coupled poromechanical simulations at finite strain. Int J Numer Anal Methods Geomech 2013;37(16):2755–88.
[56] Wang Z-Y, Jin Y-F, Yin Z-Y, Wang Y-Z. A novel coupled NS-PFEM with stable nodal integration and polynomial pressure projection for geotechnical problems. Int J Numer Anal Methods Geomech 2022;46(13):2535–60.
[57] Yuan W-H, Liu M, Zhang X-W, Wang H-L, Zhang W, Wu W. Stabilized smoothed particle finite element method for coupled large deformation problems in geotechnics. Acta Geotech 2023;18(3):1215–31.
[58] Chen Z-P, Zhang X, Sze KY, Kan L, Qiu X-M. Vp material point method for weakly compressible problems. Comput & Fluids 2018;176:170–81.
[59] Sang Q-y, Xiong Y-l, Zheng R-y, Bao X-h, Ye G-l, Zhang S. An implicit stabilized material point method for modelling coupled hydromechanical problems in two-phase geomaterials. Comput Geotech 2024;166:106049.
[60] Oñate E. Derivation of stabilized equations for numerical solution of advective-diffusive transport and fluid flow problems. Comput Methods Appl Mech Engrg 1998;151(1–2):233–65.
[61] Oñate E. A stabilized finite element method for incompressible viscous flows using a finite increment calculus formulation. Comput Methods Appl Mech Engrg 2000;182(3–4):355–70.
[62] Oñate E, Franci A, Carbonell JM. Lagrangian formulation for finite element analysis of quasi-incompressible fluids with reduced mass losses. Internat J Numer Methods Fluids 2014;74(10):699–731.
[63] Biot MA. Generalized theory of acoustic propagation in porous dissipative media. J Acoust Soc Am 1962;34(9A):1254–64.
[64] Ma K, Gao Z-q, Wang J, Zhang Y, Zong M-f, Wu W-b, Mei G-x. Nonlinear consolidation finite element analysis of a layered soft soil foundation under multistage loading based on the continuous drainage boundary. Comput Geotech 2024;169:106220.
[65] Hoppe H, DeRose T, Duchamp T, McDonald J, Stuetzle W. Mesh optimization. In: Proceedings of the 20th annual conference on computer graphics and interactive techniques. 1993, p. 19–26.
[66] Wyser E, Alkhimenkov Y, Jaboyedoff M, Podladchikov YY. A fast and efficient MATLAB-based MPM solver: fMPMM-solver v1. 1. Geosci Model Dev 2020;13(12):6265–84.
[67] De Vaucorbeil A, Nguyen VP, Sinaie S, Wu JY. Material point method after 25 years: Theory, implementation, and applications. Adv Appl Mech 2020;53:185–398.

[68] Idelsohn SR, Oñate E, Pin FD. The particle finite element method: a powerful tool to solve incompressible flows with free-surfaces and breaking waves. Internat J Numer Methods Engrg 2004;61(7):964–89.
[69] de Pouplana I, Oñate E. A FIC-based stabilized mixed finite element method with equal order interpolation for solid–pore fluid interaction problems. Int J Numer Anal Methods Geomech 2017;41(1):110–34.
[70] Xie K-H, Xie X-Y, Gao X. Theory of one dimensional consolidation of two-layered soil with partially drained boundaries. Comput Geotech 1999;24(4):265–78.
[71] Cryer C. A comparison of the three-dimensional consolidation theories of Biot and terzaghi. Quart J Mech Appl Math 1963;16(4):401–12.
[72] Xie K, Leo CJ. Analytical solutions of one-dimensional large strain consolidation of saturated and homogeneous clays. Comput Geotech 2004;31(4):301–14.
[73] Gibson R, Gobert R, Schiffman R. On Cryer's problem with large displacements and variable permeability. Géotechnique 1990;40(4):627–31.
[74] Prantle L. Uber die Eindringungsfestigkeit (Härte) plastischer Baustoffe und die Festigkeit von Schneiden. Zeit. Angew. Math Mech 1921;1:15–20.
[75] Meyerhof G. The ultimate bearing capacity of foudations. Geotechnique 1951;2(4):301–32.
[76] Navas P, Sanavia L, López-Querol S, Yu RC. Explicit meshfree solution for large deformation dynamic problems in saturated porous media. Acta Geotech 2018;13(2):227–42.
[77] Simo JC, Hughes TJ. Computational inelasticity. Springer; 1998.
[78] Kim N-H. Introduction to nonlinear finite element analysis. Springer Science & Business Media; 2014.
[79] Fish J, Shek K. Computational aspects of incrementally objective algorithms for large deformation plasticity. Internat J Numer Methods Engrg 1999;44(6):839–51.